Geoscience Frontiers 10 (2019) 629–649

Contents lists available at ScienceDirect

China University of Geosciences (Beijing)

Geoscience Frontiers

journal homepage: www.elsevier.com/locate/gsf

Research Paper

Hydrothermally induced diagenesis: Evidence from shallow marine-deltaic sediments, Wilhelmøya, Svalbard

Beyene G. Haile [a,*], Urszula Czarniecka [b], Kelai Xi [c], Aleksandra Smyrak-Sikora [d], Jens Jahren [a], Alvar Braathen [a], Helge Hellevang [a,d]

[a] Department of Geosciences, University of Oslo, Pb. 1047 Blindern, NO-0316, Oslo, Norway
[b] Institute of Geological Sciences, Polish Academy of Sciences, Twarda 51/55, 00-818, Warszawa, Poland
[c] School of Geosciences, China University of Petroleum, Qingdao, 266580, Shandong, China
[d] The University Centre in Svalbard (UNIS), Pb. 156, 9171, Longyearbyen, Norway

A R T I C L E I N F O

Article history:
Received 29 September 2017
Received in revised form
24 January 2018
Accepted 27 February 2018
Available online 3 April 2018
Handling Editor: Nick M W Roberts

Keywords:
Diagenesis
Sill intrusions
Hydrothermal convection cells
Carbonate cement
Sericitization of feldspars

A B S T R A C T

Sedimentary basins containing igneous intrusions within sedimentary reservoir units represent an important risk in petroleum exploration. The Upper Triassic to Lower Jurassic sediments at Wilhelmøya (Svalbard) contains reservoir heterogeneity as a result of sill emplacement and represent a unique case study to better understand the effect of magmatic intrusions on the general burial diagenesis of siliciclastic sediments. Sills develop contact metamorphic aureoles by conduction as presented in many earlier studies. However, there is significant impact of localized hydrothermal circulation systems affecting reservoir sediments at considerable distance from the sill intrusions. Dolerite sill intrusions in the studied area are of limited vertical extent ($\sim$12 m thick), but created localized hydrothermal convection cells affecting sediments at considerable distance (more than five times the thickness of the sill) from the intrusions. We present evidence that the sedimentary sequence can be divided into two units: (1) the bulk poorly lithified sediment with a maximum burial temperature much lower than 60–70 °C, and (2) thinner intervals outside the contact zone that have experienced hydrothermal temperatures (around 140 °C). The main diagenetic alteration associated with normal burial diagenesis is minor mechanical plastic deformation of ductile grains such as mica. Mineral grain contacts show no evidence of pressure dissolution and the vitrinite reflectance suggests a maximum temperature of $\sim$40 °C. Contrary to this, part of the sediment, preferentially along calcite cemented flow baffles, show evidence of hydrothermal alteration. These hydrothermally altered sediment sections are characterized by recrystallized carbonate cemented intervals. Further, the hydrothermal solutions have resulted in localized sericitization (illitization) of feldspars, albitization of both K-feldspar and plagioclase and the formation of fibrous illite nucleated on kaolinite. These observations suggest hydrothermal alteration at $T > 120$–140 °C at distances considerably further away than expected from sill heat dissipation by conduction only, which commonly affect sediments about twice the thickness of the sill intrusion. We propose that carbonate-cemented sections acted as flow baffles already during the hydrothermal fluid mobility and controlled the migration pathways of the buoyant hot fluids. Significant hydrothermally induced diagenetic alterations affecting the porosity and hence reservoir quality was not noted in the noncarbonate-cemented reservoir intervals.

1. Introduction

The quality of petroleum reservoirs depends strongly on the burial history and diagenesis, and understanding the processes that change the properties of reservoir rocks are therefore of economic importance. Diagenesis of sandstones involves physical and chemical processes that are responsible for changing the mineral

* Corresponding author.
E-mail address: b.g.haile@geo.uio.no (B.G. Haile).
Peer-review under responsibility of China University of Geosciences (Beijing).

https://doi.org/10.1016/j.gsf.2018.02.015
1674-9871/

composition, texture and fluid flow properties of sedimentary rocks. Diagenesis is responsible for the formation of secondary porosity, for porosity destruction through compaction and in some cases porosity preservation to great depths (Surdam et al., 1983; Bjørlykke, 1988; Ehrenberg, 1993; Salem et al., 2000; Bloch et al., 2002). Investigating the processes and products of diagenesis is thus critical for constraining rock texture, porosity and permeability during burial (Bjørlykke et al., 1979; Worden and Morad, 2000; Ajdukiewicz and Lander, 2010; Morad et al., 2010; Taylor et al., 2010; Bjørlykke and Jahren, 2012). Moreover, understanding diagenesis improves our ability to predict reservoir quality at a local scale and modeling the evolution of sedimentary basins at regional scales (Wilson et al., 2006; Zhu et al., 2006).

As the energy demand in the world is increasing, the exploration activity for hydrocarbons moves towards more challenging systems such as basins affected by magmatic activity (Senger et al., 2014, 2017; Schofield et al., 2015b). There are numerous challenges for petroleum exploration in such basins because igneous intrusions may impact diagenesis, thermal history, seismic imaging, reservoir compartmentalization, source rock maturation, and hydrocarbon migration pathways (Holford et al., 2012, 2013; Rateau et al., 2013; Jerram, 2015; Eide et al., 2017; Grove et al., 2017; Schofield et al., 2017; Senger et al., 2017). To date, basins influenced by magmatic intrusions have become a major focus for many exploration companies. It is therefore important to understand the influence of intrusion-induced diagenesis on reservoir quality in such type of basins (e.g. Vøring Basin, Faroe-Shetland Basin, the Northern parts of the Barents Sea, western Australian continental margin, and offshore Madagascar). This is essential to reduce exploration risk.

When sills intrude sedimentary rocks, heat can be transferred by conduction and/or by convection of fluids (Ferry and Dipple, 1991). Most published works associate the impact of sill intrusions in sedimentary strata to pyrometamorphism and/or contact metamorphism (Reeckmann et al., 1985; Karlsen et al., 1998; Mckinley et al., 2001; Grapes, 2010; Aarnes et al., 2011). It has however also been demonstrated that magmatic sills intruded into highly porous sediments have resulted in hydrothermal fluid mobility that influenced rock properties further from sill intrusions (Einsele et al., 1980), and also recent studies have shown that hydrothermally induced fluid migrations affect the temperature history and diagenesis in the host sedimentary rock (Schofield et al., 2015a; Angkasa et al., 2017; Grove et al., 2017; Senger et al., 2017).

Svalbard is suitable to examine the influence of heat-flux related to short-lived events of hydrothermal induced diagenesis in sandstones, as outcrops of highly porous Mesozoic sedimentary units that have been intruded by igneous rocks are abundant and well exposed. The Triassic (De Geerdalen Formation) and Lower Jurassic (Wilhelmøya Subgroup) sediments exposed at Wilhelmøya are time equivalent to subsurface rocks in the Barents Sea area (Mørk et al., 1999). The outcrops, in addition, provide information on the 3D spatial variability of sedimentary facies of deltaic and shallow marine strata and provide good insight into the depositional environment and the related spatial variability of diagenesis. They can also serve as an excellent natural laboratory to give insights about diagenetic alteration and ultimately reservoir quality evolution in the subsurface where sediments interact with sills. Furthermore, reservoir quality modifications as a result of diagenesis and documentation of this process is important because: (1) there are relatively few studies on hydrothermally induced diagenesis compared to normal burial diagenesis (Mckinley et al., 2001; Ahmed, 2002; Machel and Lonnee, 2002; Rossi et al., 2002; Ochoa et al., 2007; González-Acebrón et al., 2011; Grove, 2013; Holford et al., 2013; Grove et al., 2017); (2) despite several published papers on sedimentology, sequence stratigraphy, structural and tectonic evolution of the Barents Sea area (Faleide et al., 1993; Glørstad-Clark et al., 2010, 2011; Klausen and Mørk, 2014; Klausen et al., 2014, 2015; Anell et al., 2016; Lord et al., 2017), the impacts of diagenesis on reservoir quality evolution of the Triassic sequences is scarce (Mørk, 2013); and (3) Mesozoic outcrops at Svalbard are located in the uplifted parts of the Barents sea region which has a comprehensive burial history leading to different burial diagenesis compared to other basins.

On Svalbard, as a general trend, Mesozoic sandstones are well cemented and have low porosities and permeabilities. Contrary to this the Wilhelmøya Subgroup, as observed at the type location at Wilhelmøya, are composed of poorly lithified sediments with some thinner cemented intervals. These sediments have never been buried deeply (about <2 km), explaining the general lack of cementation. The diagenetic overprints occurring at the onset of the transition from mechanical to chemical compaction window makes the sequences at Wilhelmøya an excellent natural laboratory to investigate early chemical diagenesis. Moreover, by using diagenetic observations that enable placing constraints on the temperature of the sediments, the sequence offers the opportunity to shed new light on the uplift and temperature history of the area. Diagenetic processes, such as the onset of quartz cementation, pressure-dissolution at stylolites, and the transformation of smectites to illite occur in the same temperature range. Diagenetic fingerprints can therefore be used as indicators of maximum burial temperatures before uplift, and the extent of the uplift.

Temperature proxies may in addition be useful to better understand the effect of sill intrusions penetrating the sediments in this region and sediments deposited in similar settings. A larger part (~900,000 km^2) of the northern and eastern Barents Sea (it covers both Norwegian and Russian territorial waters) contains abundant igneous intrusions with a volume estimate of 100,000 to 200,000 km^3 predominantly in the Permian to Triassic sedimentary units across the Barents basin (Polteau et al., 2016). The sill intrusions in the study area have moderate vertical extent but have still influenced the heat budget of the area. Moreover, because sedimentary successions on Wilhelmøya have never been buried deeply, the effects of the hydrothermal alteration can easily be distinguished from the background low-temperature diagenesis. This paper examines the effect of sill intrusion-induced diagenesis compared to the normal diagenesis on sandstone reservoir properties.

2. Geological background

2.1. Svalbard geology

Svalbard is situated at the north-western parts of the Barents Shelf, bordered to the north by a rifted continental margin and to the south-west by a sheared margin (Johansson et al., 2005; Faleide et al., 2015). During the Late Cretaceous a regional uplift of the northern Barents Shelf resulted in subaerial exposure of the Svalbard archipelago (Johansen et al., 1992; Riis et al., 2008; Worsley, 2008; Dörr et al., 2012, 2013; Blinova et al., 2013). The magnitude of the uplift has been suggested to be strongest in the northern and western parts of Svalbard, however, the entire Barents Shelf region has been uplifted and eroded in the late Cenozoic (Nøttvedt et al., 1988, 1992; Vorren et al., 1991). The average thickness of the strata removed due to erosion was estimated up to approximately one km in SW Barents Sea; however, the uplift was more intense north of 75°N, and with uplift close to three km on Svalbard (Nøttvedt et al., 1992; Henriksen et al., 2011; Dörr et al., 2012).

Based on coal rank data, the subaerially exposed areas of the north eastern part of Svalbard have been subjected to an overburden of 2000 m (Mørk and Bjorøy, 1984). Similarly inferring to the organic geochemical analyses data, the northern Barents Sea

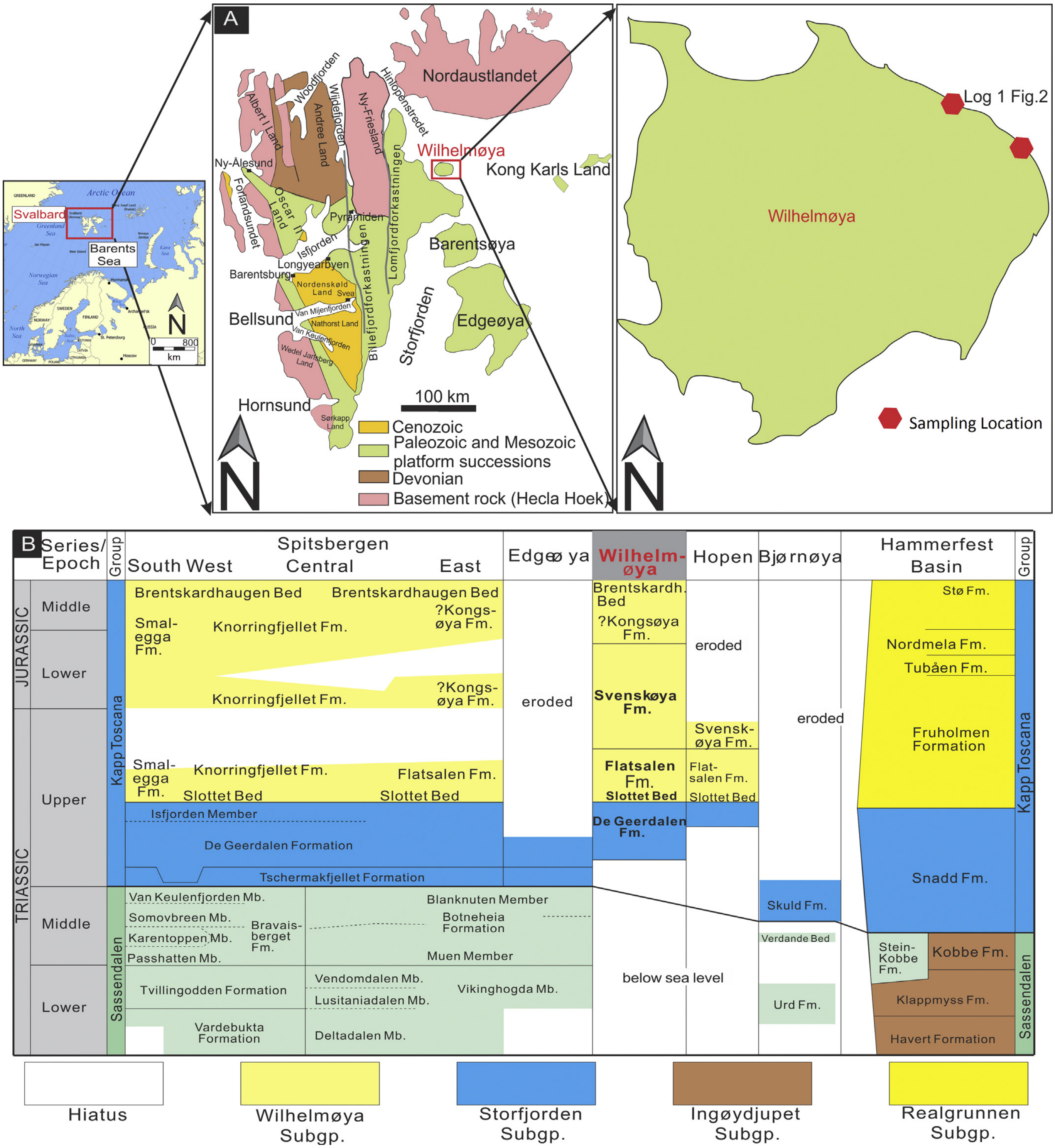

Figure 1. (A) Simplified geological map of Svalbard. The location of Wilhelmøya (Wilhelm Island) is outlined. Red hexagonal shapes depict sampling locations. The sampling location in eastern Wilhelmøya has UTM coordinates (LOG 1 site 33X 619981E and 8784911N and other site 33X 621117E and 8783543N). (B) The lithostartigraphy of Svalbard and the Barents Sea from the Lower Triassic through the Middle Jurassic. The figure is modified from Mørk et al. (1999).

(the region between Svalbard and Franz Josef Lands), the thickness of the sedimentary section removed due to erosion was almost 2000 m (Gustavsen et al., 1997). Reports based on T_{max} values of 434 °C and 436 °C from the Olga basin area located southwest of the northern Barents Sea, indicates uplift of 1900 m in this area (Antonsen et al., 1991). In the same area, based on a regional study vitrinite reflectance data revealed uplift of 1500–2000 m (Nyland et al., 1992). The magnitude of uplift increases northward up to 2000 m on Franz Josef Land compared to the center of the South Barents basin which experiences 400–500 m erosion (Sobolev, 2012). Using apatite fission track analyses, the northern Svalbard (Albert I Land, Ny Friesland and Nordaustlandet) has undergone

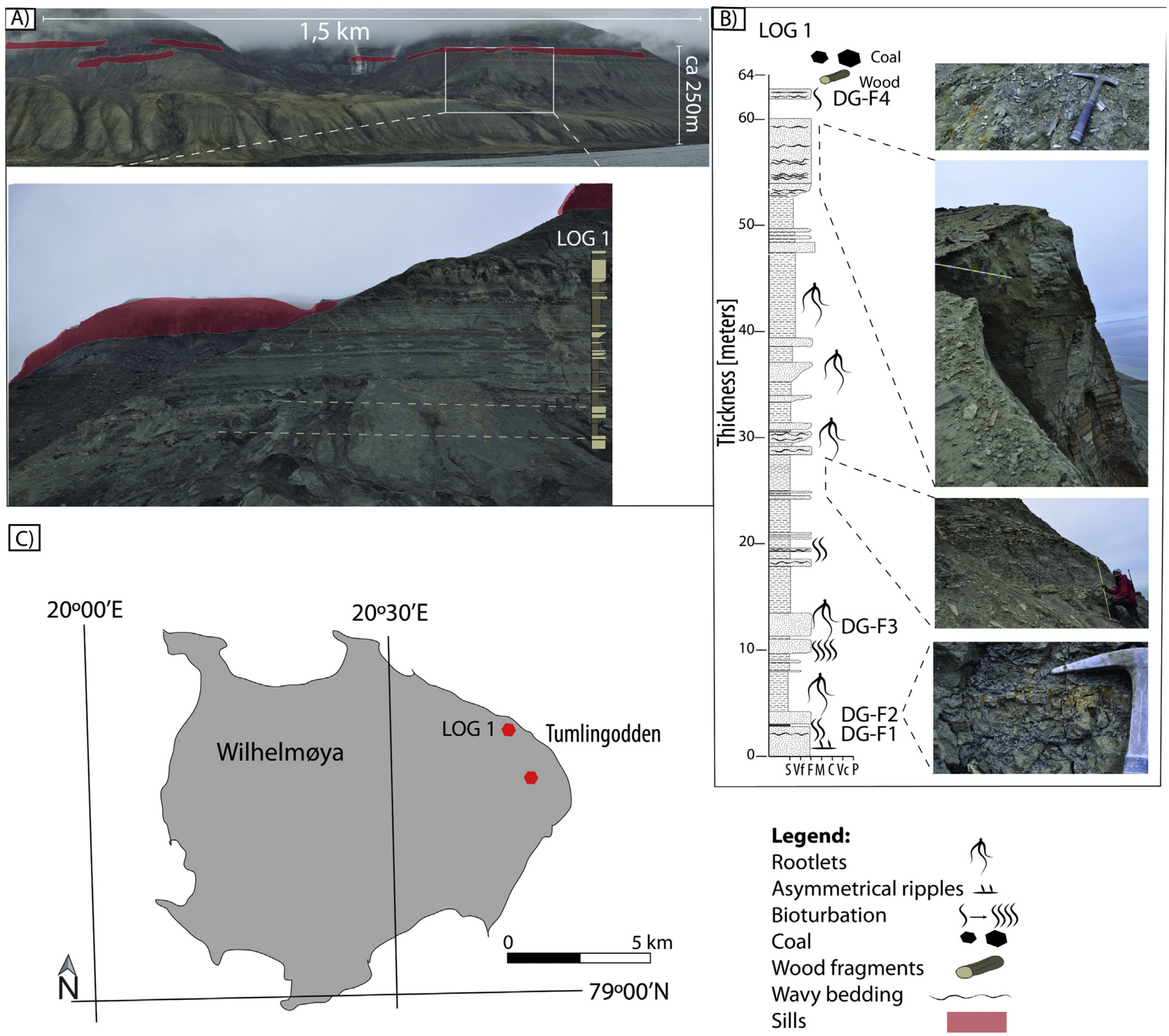

Figure 2. Sample locations and distribution of Early Cretaceous mafic sill intrusion. (A) An overview field picture showing the spatial distribution of the sill intrusion (top part) in the sedimentary strata and closer view of the lowermost sediment section where logging and sampling was done. View is westward. The sill intrusions are sub-parallel to layering. (B) Showing conventional sediment log of the lowermost succession (De Geerdalen Formation) below the sill intrusion. (C) Schematic map of Wilhelmøya showing sampling and sediment logging localities. S = silt, Vf = very fine sand, F = fine sand, M = medium sand, C = coarse sand, Vc = very coarse sand, and P = pebbles.

approximately 60 °C cooling (~120–60 °C) which is equivalent to 2–3 km at a geothermal gradient of 20–30 °C/km (Dörr et al., 2012). The aforementioned exhumation and erosion burial paleohistory estimates of the areas around the Wilhelmøya Island and the vitrinite reflectivity data have indicated that the sediments at Wilhelmøya may never been subjected to high burial temperature assuming normal geothermal gradients. It should be noted that estimates from a single thermal maturity indicator likely is uncertain, however, combining the various methods may decrease this uncertainty (Henriksen et al., 2011; Haile et al., 2018).

The basin evolution of the Svalbard archipelago began with post-orogenic subsidence of pre-Devonian basement (Caledonian orogeny and older units) during extensional collapse linked to deposition of Devonian Old Red Sandstones (Johansen et al., 1992; Blomeier et al., 2003; Braathen et al., 2017). The next major tectonic event occurred late Carboniferous rifting (Gjelberg and Steel, 1981), with a transition from broad depressions to formation of fault narrow half-grabens. The Permian was a period of tectonic quiescence which is characterized by the formation of stable marine carbonate platforms (Stemmerik and Worsley, 1989). In the late Permian, a seaway connecting East Greenland and the North Sea opened, changing the marine carbonate platforms from a hot to cold-water environment. This is seen as a transition from prevalent ramp carbonates and evaporites to mainly spiculitic limestones and shales (Worsley, 2008). During the Mesozoic (Triassic), Svalbard gradually changed its position from about 45°N to approximately 60°N (Smith et al., 1994; Ditchfield, 1997). This era was characterized by sea level rise and warm climatic conditions (Hallam, 1985), with the Svalbard climate reflecting a humid temperate domain. The Mesozoic deposits on Svalbard are mostly marine, and three main successions were deposited from Triassic to Cretaceous; the Sassendalen, Kapp Toscana and Adventdalen groups. These groups are made up of terrestrial deposits that are dissected by magmatic intrusions. During the Mesozoic period, sediments were in general siliciclastic in nature and deposited in a continental shelf setting dominated by shale and sand. There was no or little tectonic activity at the eastern and north eastern parts of Svalbard (Worsley, 2008), albeit (Anell et al., 2013) argue for some late fault activity. In contrast, the western part of the Barents Sea was a tectonically active region throughout the Mesozoic and Cenozoic times, showing comprehensive tectonic evolution characterized by several orogenic events (Faleide et al., 1984). These tectonic events affected the Barents Sea region and thus controlled the basin configurations and sedimentary responses (Gabrielsen, 1984; Mørk et al., 1989; Johansen et al., 1992; Breivik et al., 1998; Klausen et al., 2015) with the establishment of a transform fault between Svalbard and Greenland at the end of the Mesozoic. The Cenozoic saw the creation of a mountain belt in the west and a related foreland basin eastward in the central part of Svalbard. Continental to marine and back to continental sediments filled this depression, prior to uplift and erosion.

2.2. Studied stratigraphy

The samples studied here are the Upper Triassic to Jurassic Kapp Toscana Group exposures on the islands of Wilhelmøya. Wilhelmøya is an island situated in the eastern part of the Svalbard archipelago, approximately 50 km east of the main island Spitsbergen covering an area of about 120 km^2 (Fig. 1A). The island is located in the northeastern part of the eastern Svalbard platform near to the N–S oriented Lomfjorden Fault zone (LFZ) (Fig. 1A).

The Kapp Toscana Group includes sediments categorized into two main subdivisions: De Geerdalen Formation and Wilhelmøya Subgroup. Upper Triassic to Lower Jurassic sedimentary sequence comprises the Carnian to early Norian De Geerdalen Formation overlain by the Wilhelmøya Subgroup (Fig. 1B). The depositional setting for the De Geerdalen Formation and Wilhelmøya Subgroup has been interpreted to be nearshore deltaic environments. Based on detailed sedimentological studies, the De Geerdalen Formation is ascribed to a shallow marine to prograding deltaic sandstone succession (Mørk et al., 1999; Krajewski, 2008; Lord et al., 2017) while the Wilhelmøya Subgroup comprises a coastal plain and in deltaic to shallow marine platform environments (Worsley, 1973; Dypvik et al., 2002). The sandstones of De Geerdalen Formation are texturally and compositionally immature while that of Wilhelmøya Subgroup consists of mineralogically mature sand and sandstones (Mørk et al., 1999; Mørk, 2013). The Wilhelmøya Subgroup is further subdivided into the Flatsalen, Svenskøya and Kongsøya formations, with regionally defined boundaries the Slottet bed of phosphatic nodular beds occur at the base and similar phosphatic beds of Brentskardhaugen bed at the top. A major transgression in the early Norian initiated marine sedimentation of the Wilhelmøya Subgroup in Svalbard and of the correlative Realgrunnen Subgroup in the Barents Sea area (Riis et al., 2008). There is a general thickening of the Wilhelmøya Subgroup and De Geerdalen Formation towards the east (Steel and Worsley, 1984).

The sediment source areas during the late Triassic were positioned to the east, northeast, and west (Nøttvedt et al., 1992; Mørk, 1999). However, in recent studies the main source of the sediments deposited in the northeastern part of Svalbard has been suggested to be from the east, mainly sourced from the Uralian orogeny, similar to suggestions by Steel and Worsley (1984). This interpretation is based on results from detrital zircon age analyses (Bue and Andresen, 2013), clinoform geometries observed on seismic data, and seismic studies in the Barents Sea (Faleide et al., 1984, 1993, 2008; Lundschien et al., 2014), and finally sedimentological and sequence stratigraphic investigations (Riis et al., 2008; Glørstad-Clark et al., 2010, 2011; Klausen and Mørk, 2014; Lord et al., 2014, 2017; Rød et al., 2014).

The Kapp Toscana Group sandstones exposed on Wilhelmøya are intruded by magmatic sill intrusions. Large and widely spread thermal activity in the Arctic has been identified during the late Mesozoic (Maher, 2001; Nejbert et al., 2011). This activity is collectively named as the High Arctic Large Igneous Province (HALIP) (Maher, 2001). The late Mesozoic (early Cretaceous) magmatism has a widespread occurrence throughout Svalbard and is represented predominantly by sill intrusions up to 100 m thick and laterally continuous for up to 30 km. The sills studied from different parts of Svalbard contain plagioclase, clinopyroxene, alkali feldspar, Fe-Ti oxides and accessory minerals such as olivine, apatite, quartz, pyrite, chalcopyrite and bornite (Nejbert et al., 2011). Generally, similar to at other islands, the sills of Wilhelmøya are tholeiitic (Weigand and Testa, 1982). The dolerite intrusions at Wilhelmøya have an undulating morphology (Fig. 2). Unlike other islands in the archipelago, sill intrusions on this island have more abundant biotite.

3. Materials and methods

Samples of Upper Triassic to Lower Jurassic aged Kapp Toscana Group sediments were collected from well-exposed outcrops at Wilhelmøya and the lowermost sequence found below the sill intrusion was logged (Fig. 2). Sampling of the DF and WS was concentrated at two locations approximately 2–3 km apart laterally. The sampling locations based on GPS coordinates are indicated in Fig. 2. The Samples collected represent the full range of stratigraphic variation within DF and WS both from tight carbonate cemented intervals and relatively uncemented intervals. No obvious weathering effects have been observed in the sandstone strata of either DF or WS. Fresh sediment samples taken directly beneath the exposed parts of sediment surface were sampled for diagenetic, petrographic, mineralogical and geochemical analyses.

Thin sections were prepared for 16 sandstone samples; 5 from the De Geerdalen Formation and 11 from the Wilhelmøya Subgroup. Conventional petrographic analyses were made to inspect the grain size, shape and mineral composition of samples. Moreover, the crystal morphology and textural relationships between the grains and pore-filling materials at thin section scale were investigated and the diagenetic features were examined using a JEOL JSM-6460LV scanning electron microscope (SEM). The SEM coupled with an energy-dispersive spectrometer (EDS) was used to perform spot chemical analyses to obtain semi-quantitative mineral compositions. Quartz cement is often difficult to delineate clearly using optical microscope and SEM coupled with backscattered electron (BSE) images. Therefore, SEM coupled with cathodoluminescence (CL) analyses were used to differentiate quartz overgrowths from detrital quartz. Moreover, stub samples were analyzed using SEM in order to complement the thin-section study and to decipher the morphology of some clay minerals where it was not obvious in the 2D thin-section (for example illite, chlorite and kaolinite).

X-ray powder diffractometry (XRD) analyses of bulk-rock samples were performed: (1) to complement optical petrography and SEM/EDS in order to identify and quantify sandstone constituents, and (2) to guide the thin section analysis. About 3.5 g of each sample were crushed, milled in ethanol in a McCrone micronizing mill and then dried at 60 °C. Randomly oriented powders were prepared by top loading into PMMA (Polymethylmethacrylate) sample holders designed with concentric circular geometry grooved shallow wells. The powder diffraction patterns were then

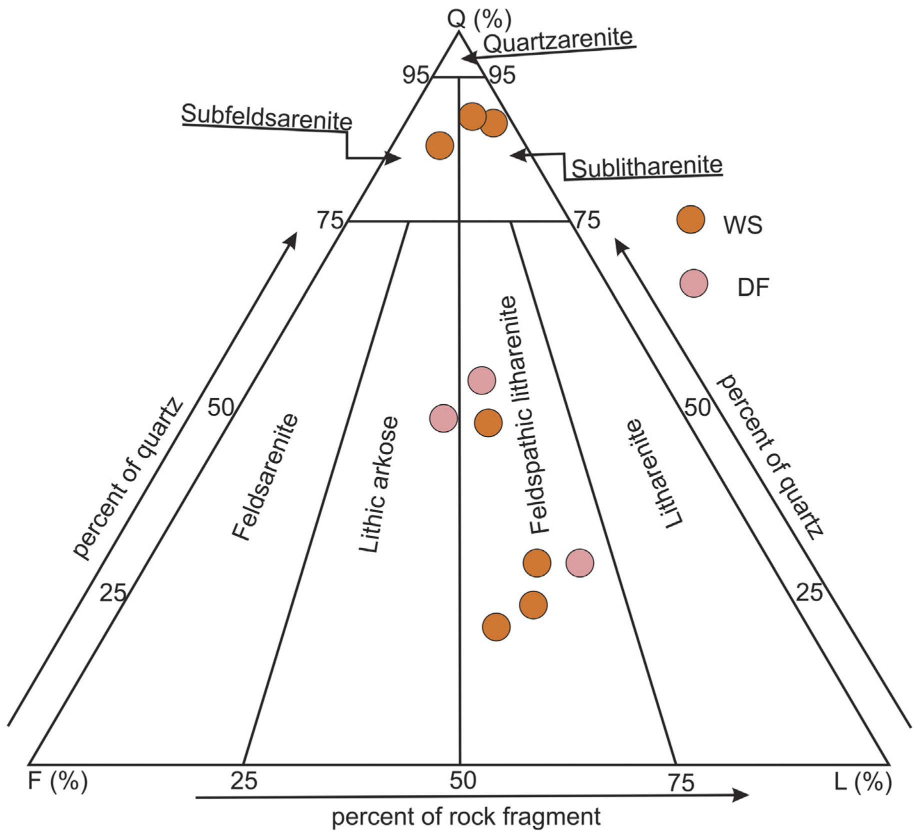

Figure 3. QFL composition of the studied thin sections; Q–quartz, F–feldspars, L–lithoclsats. The QFL triangle classification is after McBride (1963), Dott (1964), Folk et al. (1970), Williams et al. (1982), and Pettijohn et al. (2012). Petrographic point count data are presented in Appendix A. Table 1.

collected using a Bruker D8 Advanced diffractometer with Cu Kα radiation at a wavelength of 1.5406 Å. All XRD data collected were first analyzed for phase identification using the search-match module of the EVA software using the reference data bases ICDD PDF-2 and COD. After phases were identified with EVA, they were further analyzed based on the Rietveld quantitative X-ray diffraction refinement approach (RQXRD). Rietveld QXRD was performed using the Profex-BGMN-bundle software version 3.5.0 (Döbelin, 2015) and using the BGMN crystal structure files.

Vitrinite reflectance, fluid inclusion, and stable carbon ($\delta^{13}C$) and oxygen ($\delta^{18}O$) isotope analyses were performed on selected samples. One coal sample, from the Lower Jurassic strata, was analyzed for vitrinite reflectance at Applied Petroleum Technology (APT) at Kjeller, Norway, and all analytical procedures followed NIGOGA, 4th Edition (Weiss et al., 2000). Reflected light studies were carried out using polished bulk samples mounted in resin blocks, and polished isolated kerogen samples, mounted in resin on petrographic slides. Reflectance measurements were made with a Zeiss Epiplan-Neofluar 40x oil immersion objective and 10x eyepieces, with an inherent tube magnification of 1.6x giving a total visual magnification of 640x. R_0 (Random) reflectance measurements were made in non-polarized light setting. All the performed measurements were calibrated with regard to standards of known reflectance. The maximum burial temperature was estimated from R_o using: T (°C) = (ln R_o + 1.68)/0.0124 (Barker and Pawlewicz, 1994). This model was chosen because it can reproduce comparable results as that of the kinetic model developed by Sweeney and Burnham (1990). The Sweeney and Burnham (1990) kinetic model (thermal history) predictions of maximum burial temperature can be used where the burial history of the geological systems is well known.

Eight outcrop samples were prepared as polished thick sections of approximately 60–70 μm thick for fluid inclusion petrographic analyses and microthermometry measurements. Microthermometric determinations on fluid inclusions were carried out on quartz overgrowths and pore-filling calcite cement. The fluid inclusion data were collected mainly on primary inclusions using a Zeiss Axioscope A1 APOL digital transmission microscope coupled with a calibrated Linkam. TH-600 heating and cooling stage at China University of Petroleum, Qingdao, China. The instrument enables measurement of temperatures of phase transition in the range of −180 °C to 500 °C. Homogenization temperature (T_h) measurements were determined using a heating rate of 10 °C/min when the temperature was lower than 60 °C and 5 °C/min when the temperature exceeded 60 °C. The measured temperature precision for T_h is ±1 °C. The salinity data were calculated from freezing point depression in the system NaCl-H_2O for aqueous inclusions (Bodnar, 2003).

Stable carbon and oxygen analyses were made at Institute for Energy Technology (IFE) at Kjeller, Norway. Analyses were performed on four calcite-cemented sandstone samples: two from the De Geerdalen Formation and two from the Wilhelmøya Subgroup. These data are reported in per mil (‰) relative to the Vienna Pee Dee Belemnite (V-PDB) standard. The samples were heated to 400 °C for 4 h in order to remove any organic compounds. Approximately 100 μg sample was then transferred to a 10 mL vacutainer and put in a temperature controlled aluminum (Al) block. The sample was flushed with helium (He) gas for 5 min. Each bulk sample was reacted with 0.1 mL of concentrated phosphoric acid (H_3PO_4) at 30 °C for 2 h. The produced CO_2 gas (calcite fraction) was then flushed out with helium to a Poraplot Q GC column and analyses were done directly on a Finnigan MAT DeltaXP Isotope

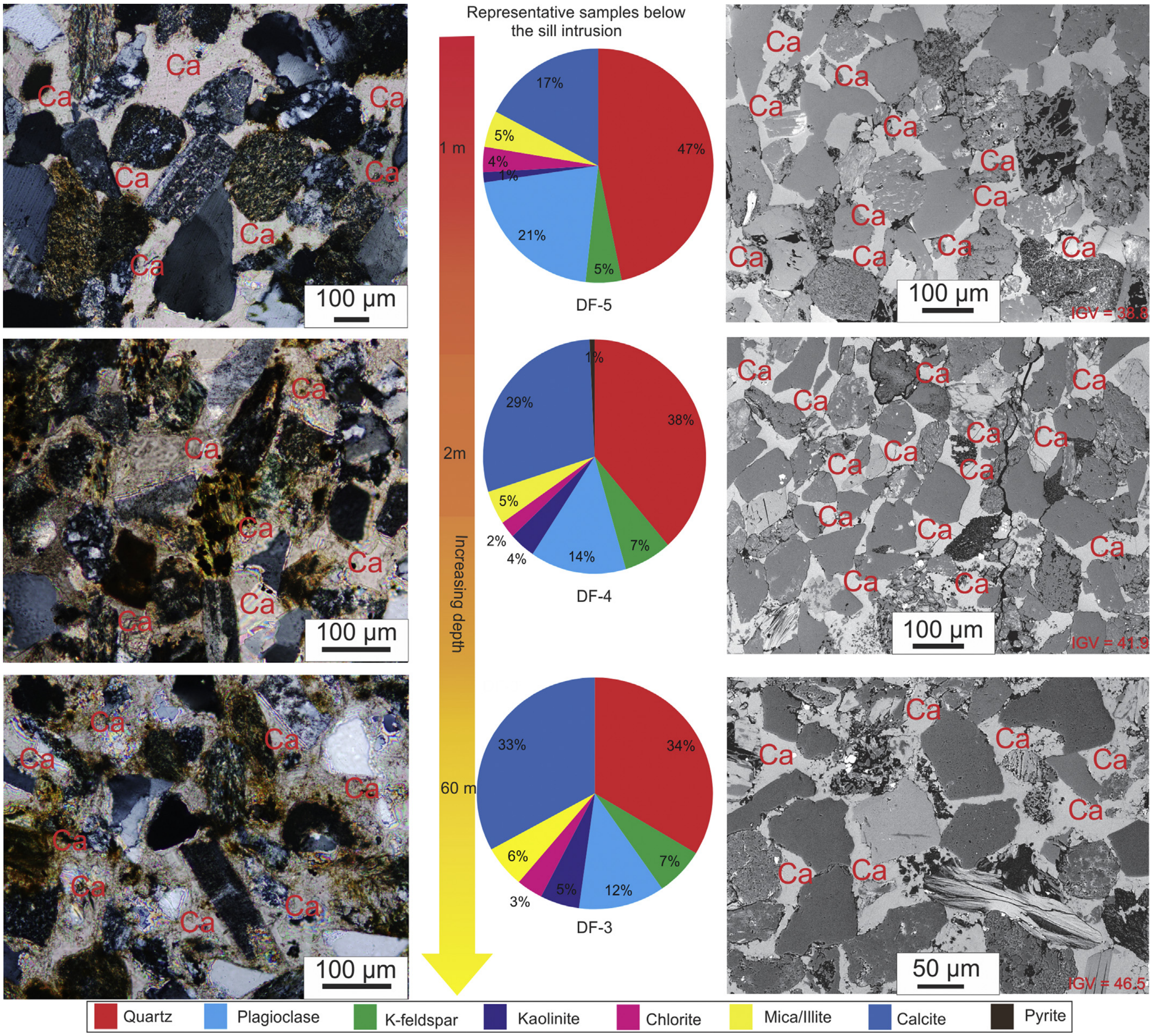

Figure 4. Thin section XPL photomicrographs, bulk XRD mineralogy and SEM photomicrographs DF samples collected from calcite-cemented intervals below the sill intrusion at Wilhelmøya. Ca = Calcite, DF = De Geerdalen Formation.

ratio Mass Spectrometer. Based on repeated analyses in the laboratory with respect to standards (V-PDB), the precision of reported results was $\pm 0.1‰$ (2σ) for both $\delta^{18}O$ and $\delta^{13}C$. Since we do not know the composition of the formation water that calcite precipitated from, we have used the equation established by Keith and Weber, (1964) that linearly relate $\delta^{13}C$ and $\delta^{18}O$ with the *Z* parameter. Z-values above 120 are classified as marine while those below 120 are meteoric (fresh) water. Calcite temperatures were calculated using the calcite-water fractionation factor equation ($1000\ln\alpha_{\text{cal-water}} = 2.78 \times 10^6\ T^{-2} - 2.89$) by assuming the water isotopic composition relative to SMOW based on the Z-value computations (Friedman and O'Neil, 1977).

4. Results

Both De Geerdalen Formation (DF) and Wilhelmøya Subgroup (WS) have sediment layers (<0.5–10 m thick) that are heavily cemented by mainly carbonates. There is apparently no relation between the frequency of occurrence and stratigraphic position of these cemented units or between cement and distance to the magmatic intrusions.

4.1. Mineralogy of the DF and WS sands and sandstones

The DF and WS sediments are very fine to medium-grained and are usually moderately well sorted, but range from well to poorly sorted. Quartz, feldspars and lithic rock fragments are the most frequent framework components. Lithic rock fragments are mainly of igneous and metamorphic origin but some sedimentary fragments are also found. Micas (mostly muscovite), glauconite, chert, hornblende and bioclasts represent other detrital grains observed. The studied sandstones are mostly feldspathic litharenites to sublitharenite, but also lithic arkoses and subfeldsarenites (Fig. 3, appendix A). DF and the lower section of

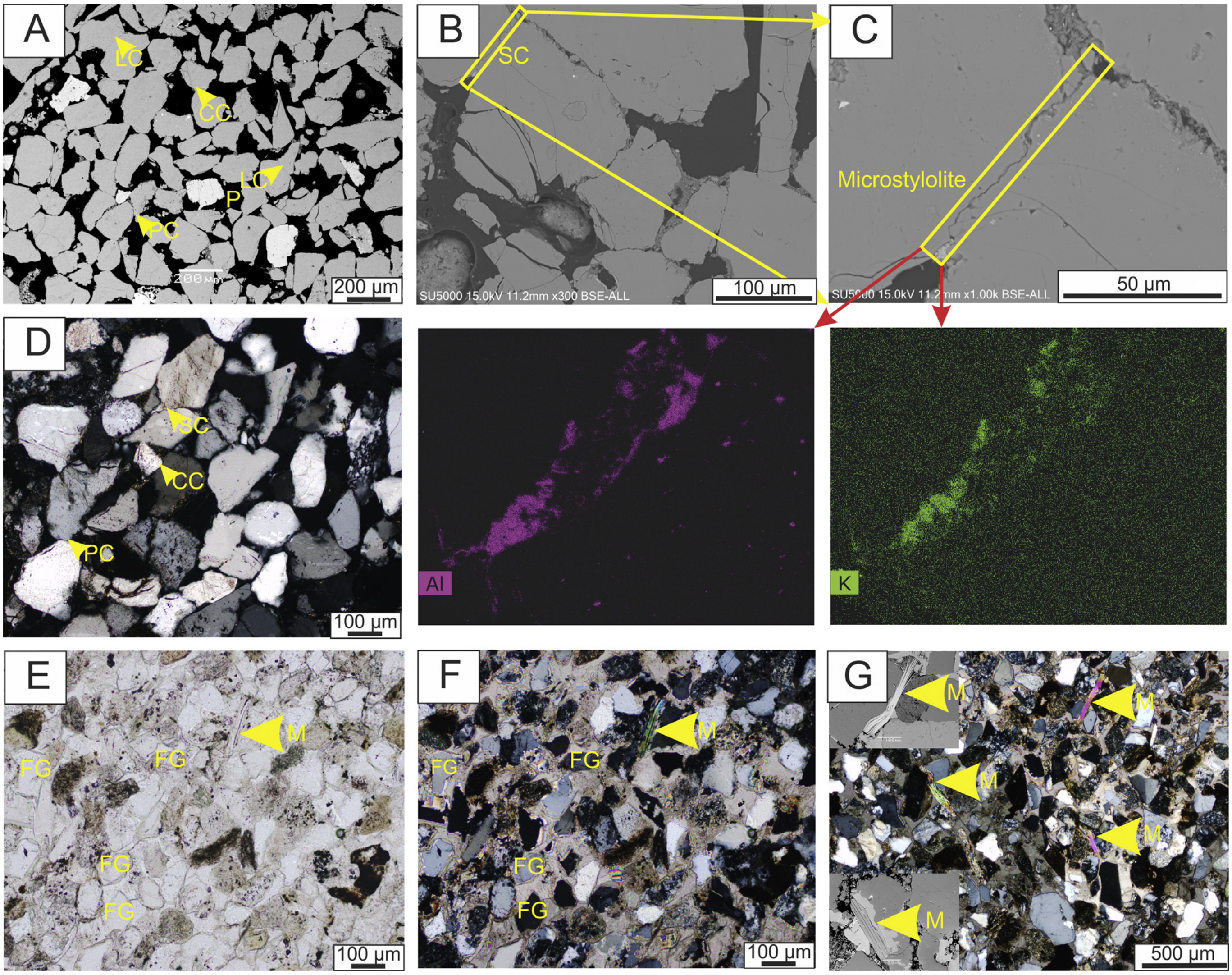

Figure 5. Some representative thin sections and SEM micrographs showing diagenetic textural features in DF and WS outcrop samples. (A) SEM micrograph of sample from intervals lacking carbonate cement displaying point, line and concavo-convex contacts between the grains. (B) SEM micrograph showing sutured contact (microstylolite). (C) Close up view of SEM micrograph of the sutured contact at "B". X-ray elemental mapping of the sutured contact shows K and Al indicating the existence of illitic material between detrital grains. (D) Photomicrograph showing sutured, concavo-convex and point contacts between the grains. (E, F) PPL and XPL photomicrograph from the same carbonate cemented units, respectively, showing floating grains engulfed with calcite cements. (G) SEM micrographs and thin section display no deformation of mica, while only minor deformation is noted. CC = concavo-convex, P = porosity, LC = line contact, SC = sutured contact, FG = floating grains, PC = point or tangential contact, M = mica, PPL = plane polarized light, XPL = cross-polarized light. Samples represented by micrographs A–D (Lower Jurassic WS), E–F (Upper Triassic DF), and G (Lower Jurassic WS).

WS (Flatsalen Formation) sediments are mineralogically immature but samples collected from the middle section of WS (likely Svenskøya Formation?) are mineralogically mature (Fig. 3). The average framework composition of this middle section is $Q_{88}F_5L_7$.

Bulk XRD quantitative analyses suggest that quartz is the main framework mineral in all of the samples. K-feldspar, kaolinite, albite, muscovite, calcite, and Fe-rich chlorite are the remaining dominant minerals, while pyrite was found in very few of the samples and gypsum only in one sample. The XRD suggest that the amount of quartz ranges from 10% to 98%, K-feldspar from 0.6% to 7.9%, albite/plagioclase from 1.2% to 21%, kaolinite from 1% to 9.4%, chlorite from 0.7% to 11%, Muscovite/illite from 1.3% to 13%, calcite from 1.2% to 86%, siderite from 8% to 46%, pyrite from 0.2% to 0.8%, and gypsum constituted about 1.5%. The results of the quantitative XRD Rietveld refinement, SEM and optical microscope micrographs of selected samples as a function of proximity to the sill are presented in Fig. 4. The amount of calcite cement in sampled carbonate cemented intervals is 17% at 1 m, 29% at 2 m and 33% at 50 m distance from the sill intrusion (Fig. 4).

4.2. Compaction

The sediment fabric is a result of mechanical and chemical compaction processes (Einsele, 2013). The most common textures resulting from compaction are sediment grains floating in cements, and tangential-, straight-, sutured-, and concavo-convex intergranular contacts (Fig. 5A–C). The DF and WS sediments exhibit dominantly point contacts and floating grains followed by long or line contacts, but a few concavo-convex and sutured contacts are also identified (Fig. 5A–D). Both, in the very porous weekly consolidated and calcite-cemented sedimentary units, mica grains show no evidence of plastic ductile grain deformation, but minor mica deformation is noted (Fig. 5G).

4.3. Quartz overgrowth

The samples belonging to DF and WS show quartz overgrowths on detrital quartz. Quartz cement includes quartz overgrowth (Fig. 6A–H) and microquartz (Fig. 6B). Microquartz occur as coatings on detrital framework grains in the WS sediments. Thin sections under an optical microscope reveal clearly the quartz overgrowths (Qo) on detrital quartz grains (Fig. 6A–H). The quartz overgrowths, however, appear to be rounded and dissolved or parts being spalled off (Fig. 6A, C–E). Quartz overgrowths can be distinguished readily from detrital quartz grains due to the presence of dust rims on detrital quartz grains (Fig. 6A–H). However, it is difficult to distinguish quartz overgrowths from detrital quartz in SEM-BSE micrographs and such distinction may also be misleading unless supported by other analytical methods. SEM-BSE display quartz overgrowths that appear euhedral (Fig. 6D). Close-up inspections of BSE micrographs however indicate that also these surfaces have been dissolved or abraded (Fig. 6A, C, and E). This is further supported by SEM-Cl micrographs (Fig. 7A–F). Quartz overgrowths (red arrows) often have very low Cl intensity or non-luminescent (appears dark) compared to the detrital quartz grains (appears bright) (Fig. 7A, D). SEM-Cl micrographs furthermore reveal a high fracture intensity of detrital quartz grains and fractures that have been healed with quartz cement (Fig. 7A, D).

4.4. Feldspar alteration

Alteration of plagioclase and K-feldspar is only found in the calcite cemented sedimentary units within DF and WS. Most plagioclase grains have been altered to some degree and pervasively leached grains are most commonly observed (Fig. 8A–C). Plagioclase leaching leaves large ($\sim$30 μm to 150 μm) secondary pores with little remnant grain material (Fig. 8A–C). Plagioclase leaching results in some albite formation within the voids previously occupied by detrital plagioclase grains. The replacement of the original detrital plagioclase grains by albite has resulted in the formation of aggregates of small euhedral albite crystals (Fig. 8A–C). Due to calcite cement, the secondary porosity formed from plagioclase dissolution is a stable void maintaining the shape of the dissolved plagioclase grains (Fig. 8A–C).

The potassium feldspars appear to be generally fresh and less altered compared to plagioclase (Fig. 8B and C). Crystallization of very thin albite rims ($\sim$2 μm) are predominantly observed around K-feldspar grains, and may indicate leaching of K^+ and recrystallization of the K-feldspar (Fig. 8A–C). The rims around K-feldspar grains are pure albite in composition and the albite crystals have abundant micro-intercrystalline porosity (Fig. 8D). In contrast to this, in the units lacking carbonate cement, there was no crystallization of albite rims observed around K-feldspar grains (Fig. 8E), likewise there was no plagioclase albitization (Fig. 8K).

Near K-feldspar grains with albite rims, fibrous illitic type clay phases occur mainly accompanied with microquartz crystals (Fig. 8F and G). These clay minerals are composed of interwoven fibrous illite bridging the pores between microquartz grains. Illitization is difficult to observe in thin-sections. However, SEM examination of the texture of authigenic illite using stub samples, show that fibrous illite nucleated and grew onto kaolinite around altered K-feldspar grains (Fig. 8H). SEM-EDS analyses of the illitic clay phase yields the major elements: K, Al, Si and O (Fig. 8F). Similar to the albite formation, illite formation is only observed in the carbonate-cemented intervals.

Plagioclase and K-feldspar alteration into sericite (illite) was recognized in the carbonate cemented layers (Fig. 8I and J), but sericite was not found associated with plagioclase and K-feldspar in sedimentary units lacking carbonate cement (Fig. 8K and L). Relict plagioclase grains show grain contacts with poikilotopic calcite cement and relict grains are sometimes engulfed by the cement (Fig. 8A–C).

4.5. Clay minerals

Kaolinite (Kao) is found in primary pores of both carbonate cemented and uncemented sandstone layers associated with mica and K-feldspar (Fig. 9A–E). Kaolinite crystals are observed between mica flakes and at the inter-fingering edges of mica (Fig. 9A–C) and also associated with relict K-feldspars (Fig. 9D–F). Replacement of mica by kaolinite was commonly observed in mica grains squeezed between rigid framework grains (Fig. 9A).

The most common clay mineral observed in addition to kaolinite is Fe-rich chlorite. SEM inspection and XRD analyses revealed that chlorite is present in all of the studied De Geerdalen Formation and the Wilhelmøya Subgroup sandstone samples. The Fe-chlorite occur as masses of interwoven flakes of small crystals ($\sim$0.2 μm) with loose internal structure arranged in a chaotic pattern at the surface of framework grains (Fig. 9G–I), but also noted as massive aggregates (orange arrows) in the pore space (Fig. 9H). However, very close to the surface of the grains, the chlorite crystals occur with parallel or slightly oblique orientation (Fig. 9I). The chlorite coats are not continuous and display thickness variations along the surface of detrital grains (Fig. 9G and H). They predominantly occur at the embayments (yellow arrows) but are absent or scarce at rounded and flat edges of the grains (red arrows) (Fig. 9G and H). SEM stub samples display the clay coatings with an overlapping flaky aggregate and ragged outlines (Fig. 9J). SEM-EDS analyses of the clay coats and rims give similar elemental composition interpreted to be primarily a chloritic-type clay in composition (Fig. 9K). There is no clear chlorite recrystallization noted (Fig. 9L).

4.6. Carbonate cements

Carbonate cements are only found sporadically in DF and WS. Some intervals, generally less than 1–2 m thick, are however heavily cemented. A closer examination of these cemented beds shows that most of the pore space is filled with calcite and siderite, and the remaining porosity is less than 4% (Fig. 10A–F). The inter-granular volume (IGV) of the cemented intervals is generally higher (around 40%) than the non-cemented intervals (Fig. 4). The sandstones are cemented by poikilotopic calcite (Figs. 4 and 10). In some parts of the sandstones, the poikilotopic calcite cement has replaced partially to pervasively the framework grains such as plagioclase (Fig. 10A, D) which resulted in the presence of oversized calcite cement. The transformation of the original carbonate cement via the dissolution of the hot focused fluids into a new and different carbonate fabric is the recrystallization we refer to backscattered SEM images. The backscattered SEM images reveal that recrystallized calcite cement dominantly fill pore spaces (Fig. 10A). Similarly, recrystallized calcite cement interfingers into quartz grains (Fig. 10C). Pervasively etched calcite cements are visible under optical microscope (Fig. 10D). Moreover, stub samples inspected under SEM display a micro-topography with dissolution pits, smooth surfaces and sharp edges unequivocally supporting textures observed under optical microscope (Fig. 10E and F). Calcite crystals display a scalenohedral pyramidal geometry (Fig. 10E and F).

4.7. Paleo-temperature proxies

4.7.1. Sediment temperature from vitrinite reflectance

The vitrinite reflectivity (VR) for coal sample in the upper part of the section was 0.30% based on 37 measurements (Fig. 11A). Based

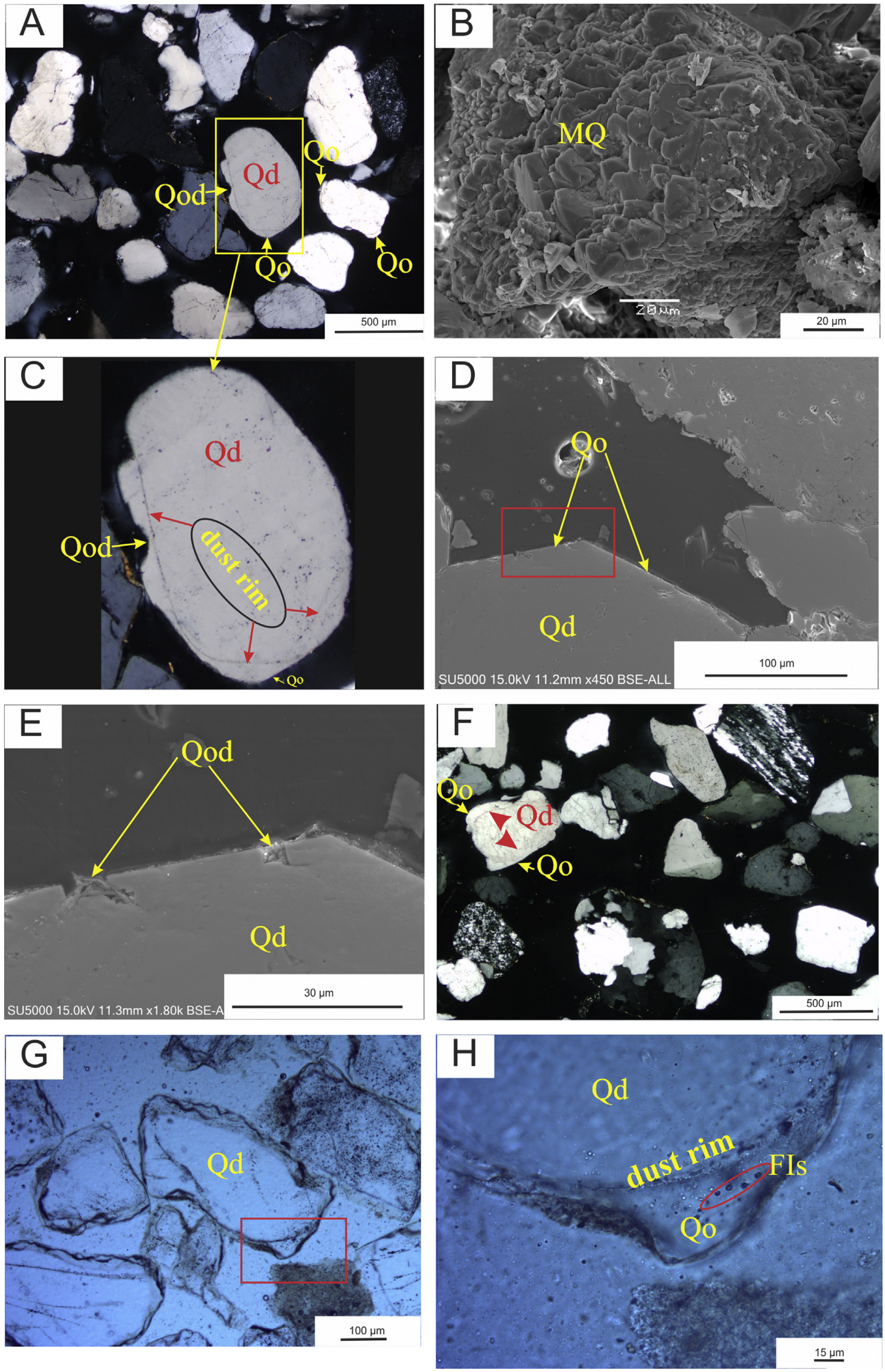

Figure 6. SEM and optical microscope cross-polarized thin section micrographs illustrating. (A) Optical micrographs of rounded quartz overgrowths (Qo) and dissolved quartz overgrowth (Qod) around detrital quartz (Qd). The sediments display well developed "dust" lines marking the boundary between the detrital quartz and overgrowth. The quartz overgrowth thickness varies from 2 to 5 µm. (B) Microquartz coating at the surface of a detrital quartz grain. (C) Closeup view of detrital quartz showing rounded and dissolved quartz overgrowth demarcated by dust rims (red arrows). (D) Quartz overgrowths that looks like euhedral crystal faces. (E) An enlargement of the area outlined by the red box in Fig. 6D reveals abrasions and breakage (discontinuous euhedral faces) quartz overgrowths or dissolved quartz overgrowths. (F) Photomicrographs of rounded quartz overgrowths

on the model of Barker and Pawlewicz (1994), this vitrinite reflectivity value corresponds to a maximum burial temperature of 38.4 °C.

4.7.2. Temperature of formation of the diagenetic phases

Aqueous inclusions for quartz overgrowths with irregular or rounded type of faces (Fig. 6) were homogenized in the range from 89.8 °C to 128.6 °C with an average temperature value of 109 °C (Fig. 11B), but these grains were most likely recycled. It was not possible to find any quartz that is without doubt authigenic with euhedral face and containing fluid inclusions. Therefore, no temperatures were therefore recorded from the authigenic quartz actually that could have formed in-situ.

Calcite cement in the heavily cemented parts contained aqueous fluid inclusions with T_h between 100 °C and 138 °C with an average value of 123 °C (Fig. 11B). The $\delta^{13}C_{V\text{-}PDB}$ values vary from −7.5‰ to −10.2‰ and $\delta^{18}O_{V\text{-}PDB}$ values range from −13.3‰ to −20.6‰ (Table 1). The Z-values were calculated based on $\delta^{13}C$ and $\delta^{18}O$ ranged from 97 to 105. The gray shaded region illustrates the possible ranges of precipitation temperatures (65–140 °C) assuming the waters involved were of meteoric origin based on the Z-values calculation with $\delta^{18}O_{V\text{-}SMOW}$ ranging from −3.5‰ to −7.5‰ (Fig. 11C).

5. Discussion

Diagenetic signatures reveal that the DF and WS sediments have been subjected to two types of thermal conditions: (1) normal diagenesis resulting in increasing temperature as a function of increasing burial depth, and (2) hydrothermal induced diagenesis from heating and focused fluid flow generated by sill intrusions. The reservoir quality in these sediments is thus a function of both low- and high-temperature diagenesis. The following section discusses the relative influence of both normal and sill induced diagenesis on present reservoir quality of these sediments.

5.1. Normal diagenesis

Ductile grains such as mica register the effects of mechanical compaction (Chuhan et al., 2002). The detrital mica being predominantly flat or undeformed to slightly bent in DF and WS sediments indicate shallow burial of the sediments before uplift. This is consistent with the types of grain contacts identified in the studied sediments. The abundance of the grain contacts being tangential and long including floating grains indicates that the sediments have been subjected to little mechanical compaction (Wilson and McBride, 1988). Concavo-convex contacts being uncommon and the existence of only incipient sutured contacts between adjacent grains indicate that the sediments underwent no or very limited chemical compaction. This is consistent with the absence of euhedral quartz overgrowths. This indicates that the sediments have not reached temperatures in excess of 60–70 °C (Walderhaug, 1994). This is in accordance with the vitrinite reflectance (VR) data translating into a temperature of about 38.4 °C (Fig. 11A). The VR is one of a number of organic thermal maturation indicators that provides the maximum temperature exposure of sedimentary rocks. However, the empirically based or kinetic translation of VR values to paleo-temperature values is still challenging. Furthermore, all the diagenetic evidence such as microquartz coatings, feldspar dissolution and precipitation of kaolinite and early calcite cementation, indicate that these sediments have not reached quartz precipitation temperatures (>65 °C) before they have been uplifted. All the above-mentioned data indicate that the sediments at Wilhelmøya have been subjected to the shallow burial depth (about < 2 km).

The quartz overgrowths identified in this study do not display euhedral shape, but are rounded and show dissolution features (Fig. 6). The existence of these rounded and dissolved quartz cements suggest that the quartz cement overgrowths were not forming in-situ but rather are inherited overgrowths, i.e. redeposited grains (Sanderson, 1984). Quartz overgrowths possibly represent remnants of cement formed at the detrital quartz surface from a previous sedimentary cycle at deep burial. This is unequivocally supported by the homogenization temperature (T_h) measurement from these quartz overgrowths. T_h ranges from 90 °C to 130 °C (Fig. 11B). The quartz overgrowth T_h values undoubtedly depart from the normal burial history of the sediments in study area.

The precipitation of microquartz crystals requires fluids with high silica supersaturation which provides a large number of small nuclei rather than few and larger crystals. Such supersaturation is most commonly provided by the dissolution of unstable biogenic silica and other small silica fossils (Williams et al., 1985; Taylor et al., 2010). The most commonly cited biogenic precursor phase for the growth of microcrystalline quartz, for instance in the Upper Jurassic reservoir rocks from North Sea, is sponge spicules (Aase et al., 1996). However, spongy spicules have not been observed in these samples during optical microscope and SEM investigations. At this stage, it is not clear what was the source of microcrystalline quartz.

As noted in this study, most of the kaolinite was pore-filling while occasional kaolinite crystals were observed between mica flakes and at the inter-fingering edges of mica. Authigenic kaolinite is in general the alteration product of feldspars and micas at shallow burial depth related to flushing by meteoric waters either during early diagenesis or after structural inversion (Bjølykke, 1980). Similarly, the authigenic kaolinite observed in DF and WS sandstones have formed as a consequence of feldspars and micas dissolution by meteoric water.

Authigenic chlorite may be formed locally as a replacement of reactive grains such as volcanic rock fragments (VRF), and transformation of the precursor clay minerals such as berthierine (Aagaard et al., 2000; Haile et al., 2015). Recrystallized authigenic chlorite coating form mainly from iron-rich precursor clay phase and will show a perpendicular orientation relative to the grain surface. Well-developed crystals having euhedral morphology will therefore commonly be arranged in an edge-to-face stacking pattern (Wilson and Pittman, 1977; Pittman et al., 1992; Grigsby, 2001; Haile et al., 2015). Moreover, such radial authigenic chlorite coats are often thick and continuous on the detrital grain surfaces. However, in this study, the chloritic clay coats are: (i) attached tangentially at the surface of detrital framework grains, (ii) patchy and discontinuous, sparsely distributed at rounded and flat surfaces but thick at the embayments in the form of loose aggregates, and (iii) the chlorite crystals are poorly-developed. These evidences indicate the detrital nature of the origin of the chloritic-type clay coats (Wilson and Pittman, 1977; Moraes and De Ros, 1990). SEM-BSE micrograph of the stub sample show overlapping flaky aggregates with ragged outlines oriented nearly tangential to the surface of the grains (Fig. 9J) is also another clear evidence suggesting the detrital origin of the clay phase covering the surface of the grains (Moraes and De Ros, 1990). Recrystallization of chlorite coats take place above about 80 °C (Aagaard et al., 2000). This will in most

(Qo) around detrital quartz (Qd). (G) Micrograph showing rounded quartz overgrowth (Qo) on a detrital quartz grain (Qd) where fluid inclusion analyses were performed. (H) An enlargement of the area outlined by the red box in Fig. 6G that reveals rounded quartz overgrowths and fluid inclusion associations in the quartz overgrowth. Samples represented by micrographs D–E (Upper Triassic DF) while the rest are (Lower Jurassic WS).

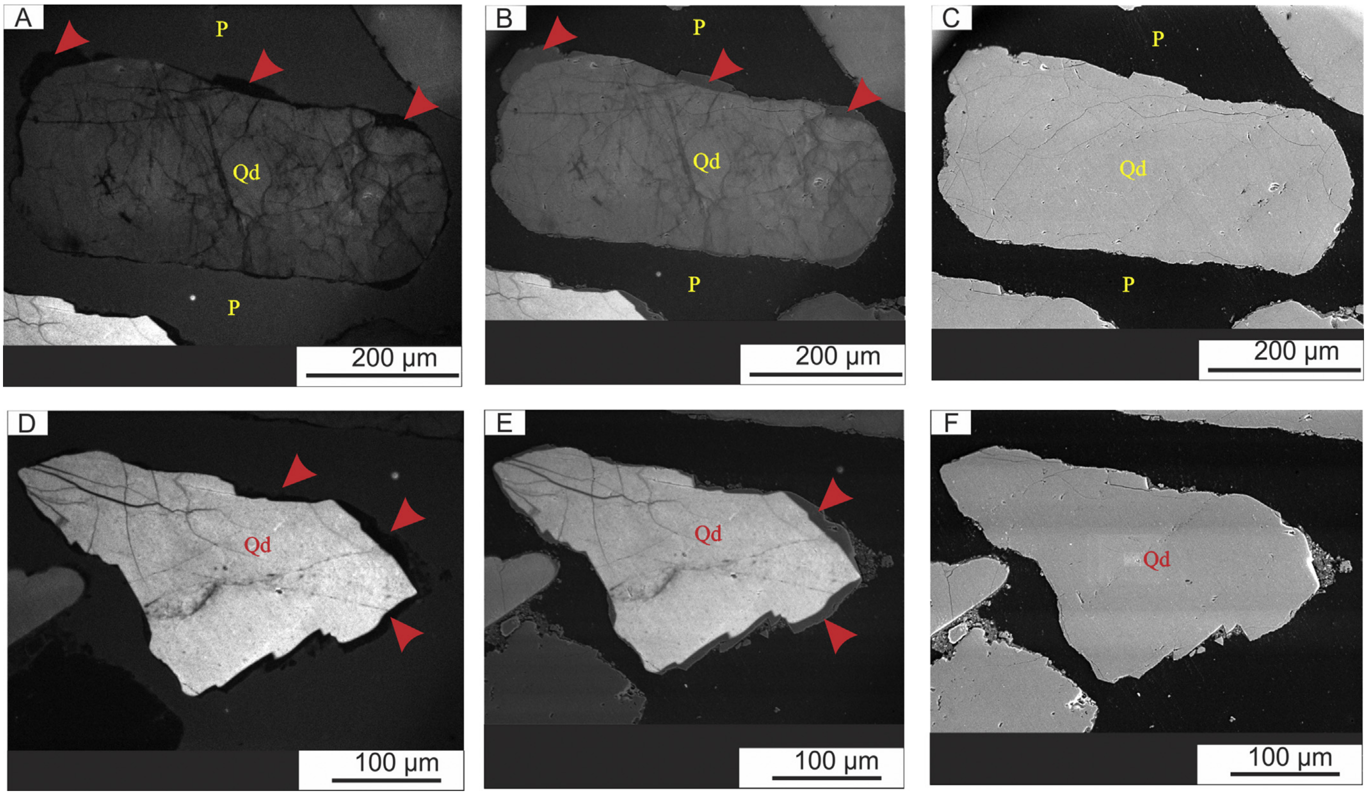

Figure 7. SEM-Cl images of detrital and authigenic quartz. (A–F) SEM-Cl, Cl-SE combined, and SE micrographs, respectively showing rounded and dissolved quartz overgrowths around two different types of detrital quartz grains, marked by red arrows. The CL micrographs display authigenic quartz filling the fracture in detrital quartz grain. P = pore space. Samples represented by micrographs A–F (Lower Jurassic WS).

cases result in growth of radial chlorite crystals on top of the tangential precursor towards the pore. This will often result in a brighter BSE greyscale image towards the pore space compared to the grain side because the recrystallized chlorite contain more Fe. Fig. 9L indicates no such chlorite recrystallization indicating that the chlorite coats never reached temperatures approaching 80 °C. Usually recrystallization of chlorite coats above 80 °C result in a brighter (more Fe) BSE greyscale image towards the pore space compared to the grain side. Fig. 9L indicates no such recrystallization indicating lower temperature than about 80 °C (Ehrenberg, 1993; Aagaard et al., 2000; Worden and Morad, 2003).

5.2. Evidence of hydrothermal induced diagenesis

Hydrothermal fluids have an effect on porosity and permeability evolution in reservoir rocks and the thermal maturation of source rocks (Karlsen et al., 1998; Ochoa et al., 2007; Holford et al., 2013; Senger et al., 2014; Grove et al., 2017). There have been discussion in the literature regarding the criteria necessary to identify ancient hydrothermal heating events based on geochemical reaction signatures (e.g. Machel and Lonnee, 2002). In sedimentary sections with anomalously high paleotemperatures compared to burial history models, geochemical reactions may be used to identify the influence of hydrothermal systems (Ochoa et al., 2007). However, in this study, sill-induced hydrothermal diagenetic processes can unequivocally be separated from normal diagenesis, because: (i) The sediments at Wilhelmøya were only at shallow burial depths before uplift (Mørk and Bjorøy, 1984) and (ii) the diagenetic signatures studied herein and also the vitrinite reflectance data show only shallow burial processes, except for the carbonate cemented layers.

5.2.1. Diagenetic fingerprints in the carbonate cemented sedimentary units

In the carbonate cemented sedimentary units diagenetic evidence, such as sericitization (illitization) of feldspars, feldspar albitization, and fibrous illite formation, suggest more different diagenesis than the normal burial diagenesis. Sericitization (illitization) of feldspar grains in cemented intervals further strengthens the interpretation of local hydrothermal alteration (Meunier and Velde, 1982; Que and Allen, 1996). The replacement of feldspar by sericite (illite) occurs when hydrothermal fluid temperatures reaches above 100 °C (Verati and Jourdan, 2014).

The IGV values for the carbonate-cemented intervals are high and the presence of floating framework grains and straight flat mica grains engulfed by carbonate cement without any sign of deformation indicate an early near surface formation (before significant burial compaction) of the calcite cement. Therefore, the calcite fluid inclusion data, giving homogenization temperatures, between 100 °C and 138 °C reflect hydrothermal induced recrystallization of calcite. Calcite cements show pervasively etched micro-topography with dissolution pits and smooth surfaces with sharp edges (Fig. 10D–F). This suggests the dissolution-reprecipitation process that took place when hydrothermal fluids were focused around the carbonate-cemented units. Hellevang et al. (2017) documented calcite crystals with similar morphology grown at high temperature laboratory experimental conditions. The precipitation-dissolution processes take place as a result of competitive environment for divalent ions between clay minerals and carbonates (Hellevang et al., 2017). In the experimental study (Hellevang et al., 2017), similar to the natural setting reported herein, the newly formed calcite crystals display both etched and euhedral crystal outlines (see Fig. 2 in Hellevang et al., 2017).

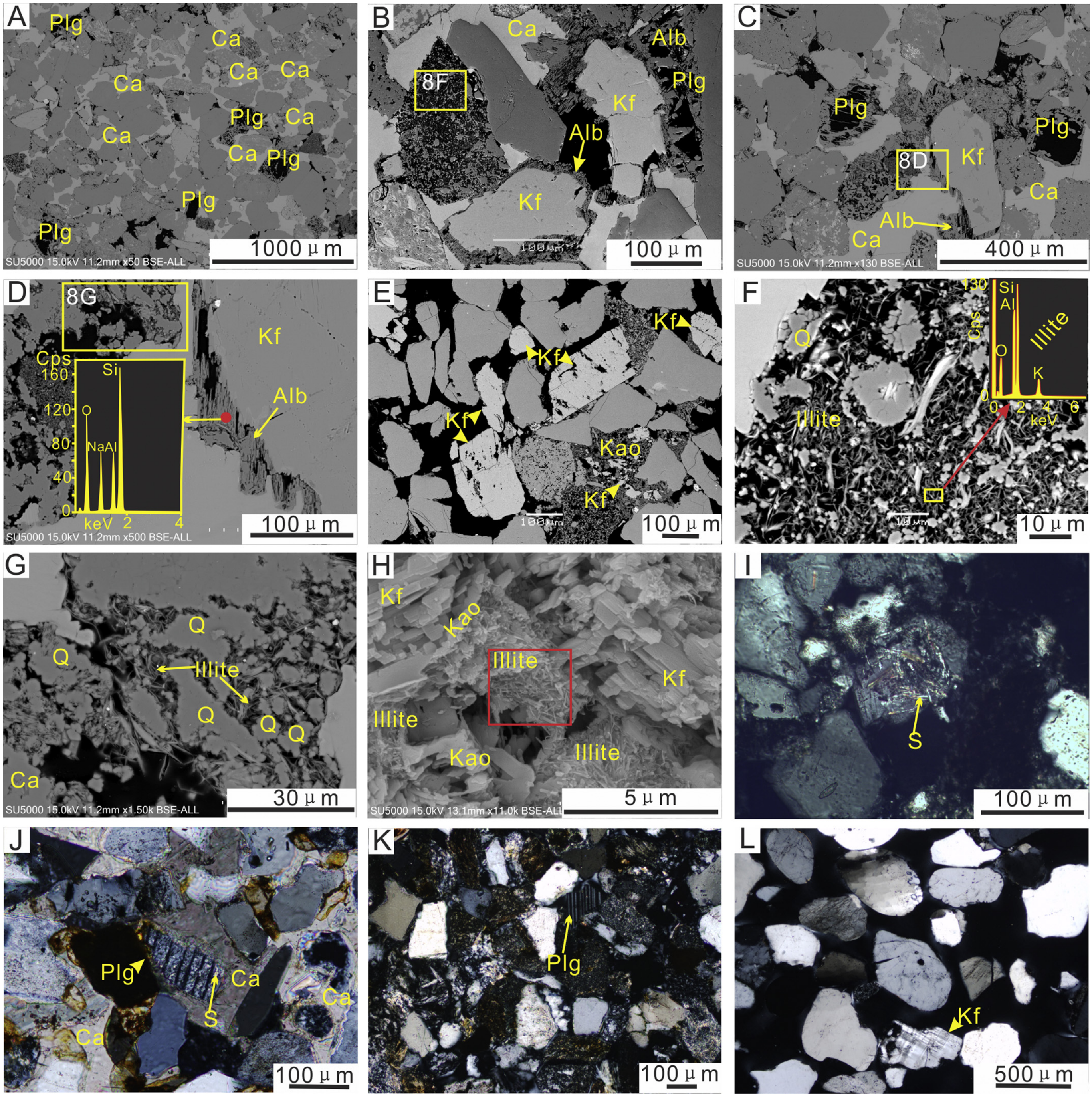

Figure 8. SEM and cross-polarized light (XPL) micrographs showing the extent of feldspar alteration. (A) Intensive leaching of plagioclase in carbonate cemented sedimentary units. (B, C) Albite rims around unaltered feldspar grains and tiny ($\sim< 1$ μm) euhedral albite crystals growing within leached plagioclase grains within a calcite cemented sedimentary unit. (D) Albite rims around K-feldspar and its texture with dissolution front noted on K-feldspar grains. Albite rims occur as crystals perpendicular to the surface displaying a palisade type texture. (E) Some K-feldspar grains show no evidence of albitization while minor and intensive dissolution of K-feldspar were noted. (F, G) An enlargement of the area outlined by the yellow box in Fig. 8B and D, reveals fibrous illitic clay in between quartz crystals in completely transformed grain at the vicinity of albite rimmed K-feldspar. The identification of original grain is virtually impossible. (H) Stub sample displaying illitic fibers grown at the edges of small crystals of kaolinite in the pore space associated with remnants of K-feldspar. (I, J) Feldspar sericitization (illitization) within calcite cemented units. (K, L) Absence of feldspars sericitization (illitization) within calcite uncemented sedimentary units. Plg = plagioclase, Ca = calcite, Alb = albite, Kf = K-feldspar, Kao = kaolinite, Q = quartz, S = sericite, spectra of inset D is albite while spectra of inset C is illite. Samples represented by micrographs A–D and F–H (Upper Triassic DF) while E and I–L (Lower Jurassic WS).

The analyzed calcium carbonates are depleted in ^{13}C with $\delta^{13}C_{V\text{-}PDB}$ values ranging from −7.5‰ to −10.2‰. The carbon isotope values may suggest derivation of dissolved carbon either from oxidation of methane or microbial sulphate reduction. Moreover as documented in Grove et al. (2017), this carbon isotope value may suggest magmatic carbon. The carbon isotope values of this study are not definitely from oxidation of methane even though likely from bacterial sulphate reduction. Sulphate reduction reaction drives alkalinity and often produces pyrite. The majority of cemented beds lack however, correlation between the calcite cement and pyrite content, which precludes the importance of sulphate reduction. The carbon isotope compositions of calcite

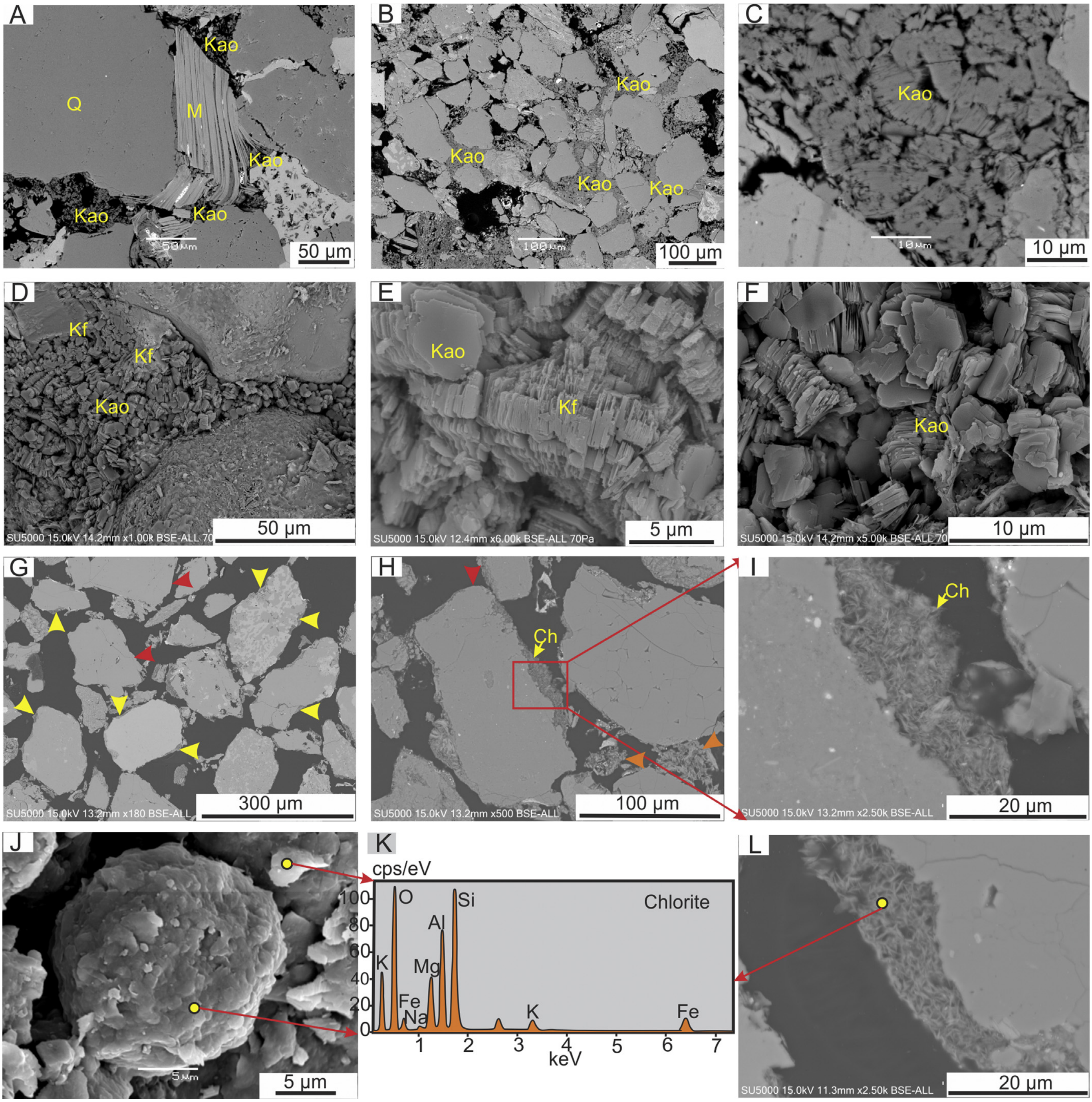

Figure 9. SEM micrographs showing pore-filling authigenic kaolinite and chlorite coats. (A) Splaying mica (M) grains with intercalated neoformed kaolinite (Kao). (B) Abundant pore-filling authigenic kaolinite. (C) Closer view of pore-filling kaolinite (Kao) at "B" associated with relict of muscovite. (D, E) Pore-filling kaolinite (Kao) associated with relict of dissolved K-feldspars (kf). (F) Closer view of pore-filling kaolinite associated with K-feldspar leaching. (G, H) Immature crystals of chlorite (Ch) rims on the surface of framework grains. (I) Pore filling immature crystals of chlorite with similar texture as that of chlorite rims on the surface of framework grains. (J) BSE micrograph of Stub sample showing the texture of chloritic-type clay mineral coatings. Poorly developed chloritic type coatings attached parallel to the detrital grain surface. (K) SEM-EDS of clay coat from stub sample and rims from thin section sample shows similar elemental composition that fits well with chloritic-type clay. (L) Thin section sample showing the texture of Clay rims around detrital sediments. Samples represented by micrographs A, G–L (Lower Jurassic WS) while B–F (Upper Triassic DF).

samples ($\delta^{13}C$ of −7.5‰ to −10.2‰) are not indicative of a specific source of the bicarbonate ion. These values could result from precipitation in pore waters bicarbonate ions supplied from two sources. Alternatively, the carbon isotope composition could reflect the dissolution, equilibration and re-precipitation, of in situ carbonate cements with a single CO_2 isotopic composition produced during hydrothermal invasion resulting from sill intrusions (Grove et al., 2017). The Z-values for the paleowater ranged from 97 to 100 suggests that calcite precipitated from meteoric water rather than saline water, but this may be highly uncertain. The $\delta^{18}O$ values of calcite cements (−13.3‰ to −20.6‰) indicate precipitation at temperatures of approximately 65 °C to 140 °C (Fig. 11C). The range obtained may reflect variations in diagenetic zones (normal burial diagenesis and hydrothermal induced diagenesis) or variations in

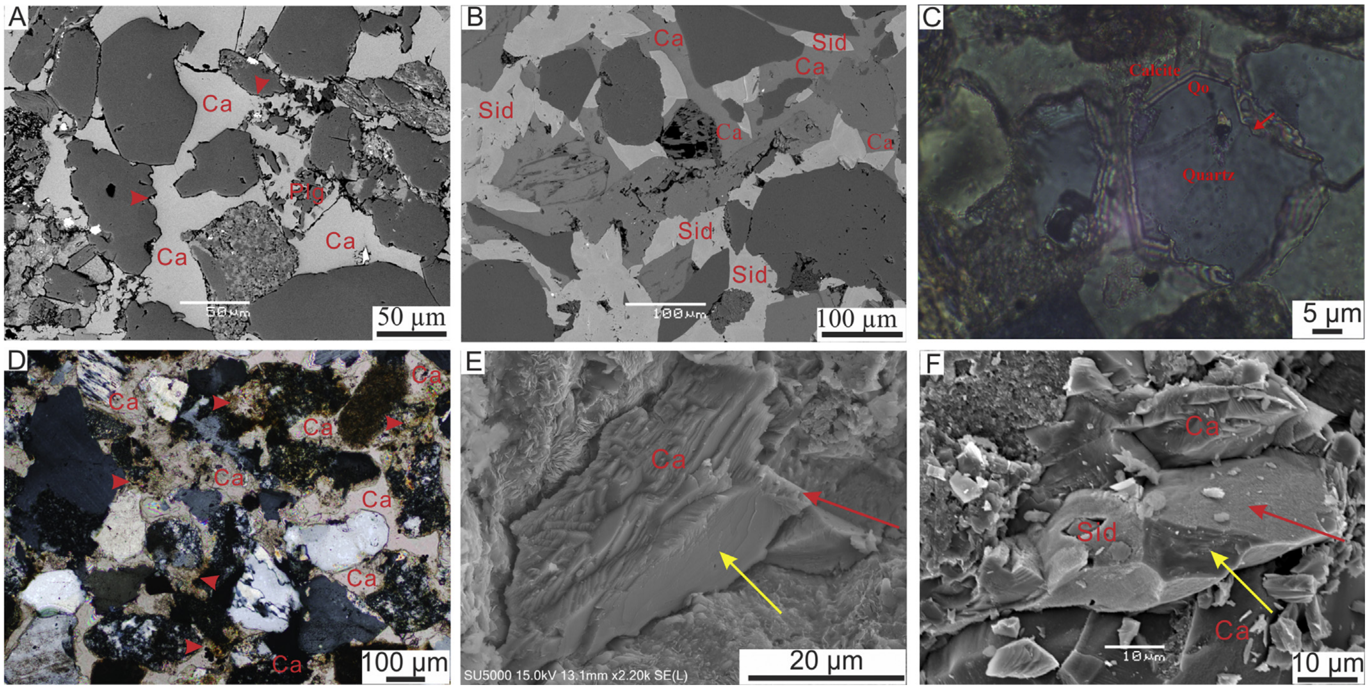

Figure 10. SEM and optical micrographs showing the nature of carbonate cements at thin-section scale. (A) Backscattered electron (BSE) micrograph of recrystallized poikilotopic calcite cement (Ca) filling pore spaces displaying dissolution fronts on quartz grains. Poikilotopic calcite cement has replaced plagioclase (Plg). (B) BSE micrograph showing pores completely carbonate cemented with calcite (Ca) and siderite (Sid) with no apparent quartz cement. (C) Thin section micrograph under XPL showing interfingering (red arrow) of quartz and recrystallized calcite cement (Ca). (D) Thin section micrograph under XPL showing recrystallized poikilotopic calcite cement. Zones where etched calcite is designated by red arrows. (E) Stub sample micrographs of BSE displaying carbonate cements occluding the pore space. The carbonate crystal displays a scalenohedral pyramidal geometry. The calcite crystal show sharp edges along with smooth surfaces (yellow arrow) and rough surfaces with itch pits or dissolution front (red arrow). (F) Stub sample micrographs of BSE displaying carbonate cements whereby siderite engulfed by calcite. The surface of siderite shows predominantly etch pit (dissolution features) outlines (red arrow) but also smooth surfaces (yellow arrow). Qo = quartz overgrowth, XPL = Cross-polarized light. Samples represented by micrographs A, C and E (Upper Triassic DF) while B, D and F (Lower Jurassic WS).

$\delta^{18}O$ of the original pore waters during early diagenesis due to fluctuations in dry or wet periods or the carbonates were affected by multiple thermal pulses during the emplacement of the magmatic sills. Most likely the temperature and isotopic composition range obtained in this study is a result of water percolation resulting from a sill intrusion induced hydrothermal convection cell.

The origins of the carbonate-cemented zones in the sedimentary strata are not clear, however, they may be derived from: (1) dissolution products of unstable Ca- and Mg-bearing non-carbonate minerals and (2) reprecipitation of dissolved bioclastic particles (Fig. 12A–D). The existence of layers composed mostly of bivalves (Fig. 12D) indicate that at least some of the carbonate layers may be derived from dissolution of mineralogically unstable bioclasts which are predominantly bivalves (Fig. 12A–D). Accumulated bivalve assemblages can easily be transported and redeposited in layers (Fig. 12D, the bottom part). This part of the section as shown in Fig. 12, is the conglomeratic Slottet member of the Wilhelmøya subgroup, and it contains phosphate mineral nodules in addition to bivalves. Bivalves are not, however, restricted to this bed, rather observed associated with carbonate cemented units in the sedimentary succession.

There was no sign of albitization of plagioclase and K-feldspar in sedimentary units lacking carbonate cement, however, in the calcite-cemented intervals the K-feldspar and plagioclase grains have been albitized. The absence of feldspar albitization in the majority of the sedimentary units except in the carbonate-cemented intervals suggest that the host sediments have not reached the feldspar albitization temperature window.

Plagioclase is preferentially albitized compared to K-feldspar (Morad et al., 1990), whereby albite crystals predominantly exist in the voids left by dissolved detrital plagioclase. Albite grains exist mainly as aggregates of euhedral albite crystals that replace the detrital plagioclase grain. Albite is formed mainly as very thin rims on K-feldspar grains. The replacement appear to be pseudomorphic within K-feldspar while mainly non-pseudomoprhic in the plagioclase. This suggests that the mechanism of plagioclase and K-feldspar albitization processes are quite different. The very thin albite rims found on K-feldspar grains may signify the low abundance of secondary potassium sinks observed. Apparently, small amounts of fibrous illite formed locally associated with kaolinite and dissolved feldspar. This chemical environment may have stabilized K-feldspar and thus restricted the albitization process.

Albite formation as a replacement of plagioclase starts when the temperature is higher than about 75 °C (Boles and Ramseyer, 1988; Morad et al., 1990), but the minimum temperature of plagioclase albitization is still poorly constrained. The albitization of K-feldspar is commonly associated with illitization of kaolinite at greater burial depths and temperatures above about 125 °C (Morad et al., 1990). The calcite-cemented intervals in the studied sandstones reveal evidence of fibrous illite formation related to kaolinite. This indicate that the sediments may have been subjected to a high temperature event transforming kaolinite to illite. However, illite may also be formed from smectite at temperatures above about 60–70 °C (Hower et al., 1976; Bjørlykke and Jahren, 2015). Morphologically diagenetic illite show a lath-shaped texture that resembles the precursor smectite (Bauer et al., 2000). Fibrous illite on the other hand, is normally only found at high temperatures

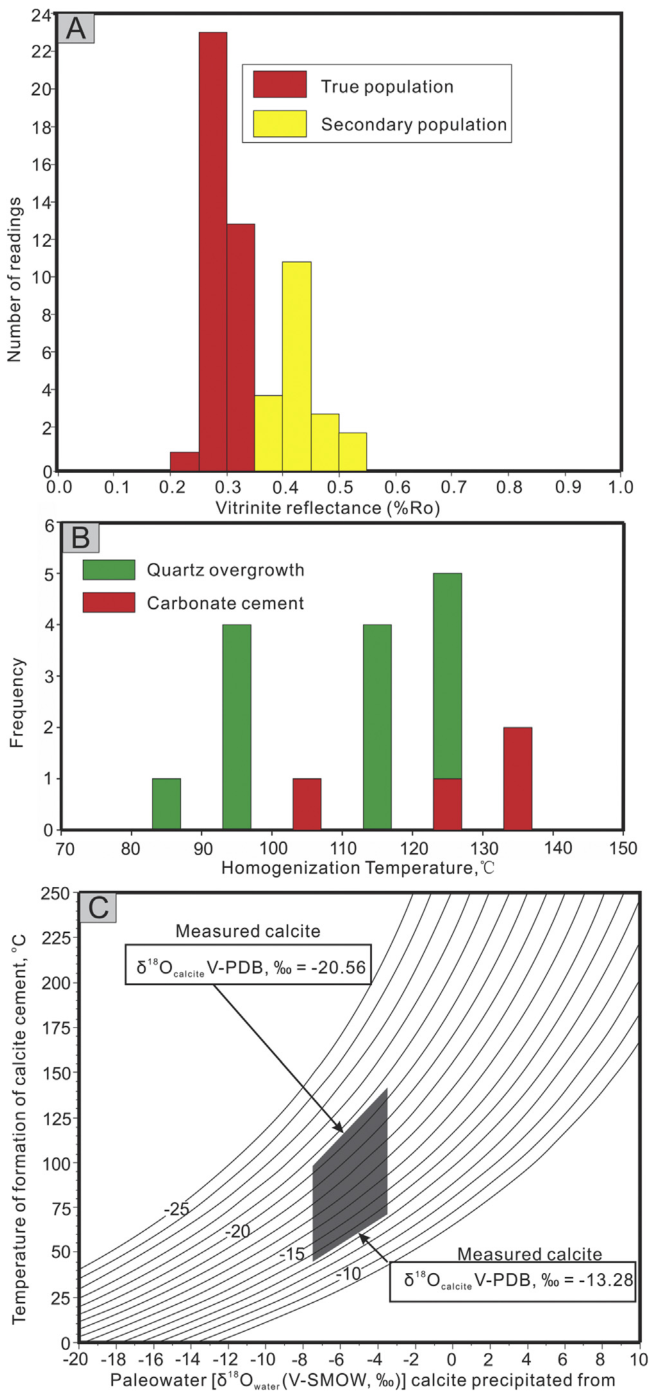

Figure 11. Plots showing paleotemperature proxies. (A) Histogram showing vitrinite reflectance (% Ro) data of coal samples with two population types: a true population (indigenous population of vitrinite) and a secondary population (population of vitrinite that may represent either oxidation or effects of mineralization). As indicated in the plot, the true population has a vitrinite reflectivity of 0.30% Ro from 37 measurements while the secondary population (higher reflectivity population) comprises 20 measurements. There was little morphological difference between the particles from the two populations, but the true population material occurred as particles in isolation. (B) Frequency distribution histogram of homogenization temperatures (T_h) for fluid inclusions in authigenic cements of outcrop samples. T_h for the aqueous inclusions found in quartz cement varies between 89.8 °C and 128.6 °C with a mean value of 109 °C whereas T_h for the aqueous inclusions in calcite cement varies between 100 °C and 138 °C with a mean value of 123 °C. (C) Plots of the equilibrium oxygen isotope fractionation between calcite and water as a function of temperature. The Z-value calculations suggest precipitation of calcite from meteoric pore waters. The Z-value calculations were based on Keith and Weber (1964). The gray shaded region illustrates the possible ranges of precipitation temperatures if the waters involved were of meteoric origin ($\delta^{18}O$ $_{V\text{-}SMOW}$ ranges between −3.5‰ to −7.5‰). The isotopic composition of calcite is illustrated as contours. Calcite temperatures were calculated using Friedman and O'Neil (1977) the calcite-water fractionation factors equation ($1000\ln\alpha_{\text{cal-water}} = 2.78 \times 10^6\,T^{-2} - 2.89$) by assuming the water isotopic composition relative to SMOW based on the Z-value computation.

(>120 °C), as the energy barrier of nucleating these crystals are high on e.g., kaolinite (Wilkinson and Haszeldine, 2002; Lander and Bonnell, 2010). Fibrous illite in this study was only found locally together with the other evidence of hydrothermal alteration, further pointing to alteration along localized features (e.g., flow baffles). This suggests that the calcite-cemented sedimentary units of DG and WS have been affected by processes deviating from the normal burial diagenesis trend in the study area.

5.3. Mechanism of the hydrothermal induced diagenesis

Abnormally high temperature authigenic phases were distinguished in the calcite-cemented intervals both above and below the sill intrusion at distances up to more than five times the thickness of the sill. The conductive mechanism commonly used to explain heat transport away from sill intrusions fail to explain this observed diagenetic pattern. Instead, an explanation invoking that the formation of thermal convection hydrothermal cells can take place in a sedimentary basins consisting of interbedded highly porous-permeable sediments and semi-permeable or impermeable layers such as shale or calcite-cemented units (Genthon et al., 1990). Such cells may form focused flows along the flow baffles, limiting the high temperature alteration to these narrow zones.

Magmatic sills intruding into reservoirs rocks may change the petro-physical properties of the reservoir rocks intruded. Mobilization of hydrothermal fluids setting up convective fluid flow cells may affect strata located a considerable distance away from magmatic activity. The fluid flow will follow the most permeable sandstone strata or along permeable faults or fracture zones (Wilson et al., 2007).

There are several indications that calcite cemented intervals of the sediments have been subjected to higher temperatures. This is shown by the sericitized feldspars, albitized feldspars, carbonate fluid inclusions, and fibrous illite formation associated with kaolinite and relict feldspar, all pointing to hydrothermal alteration (T > 120–140 °C). The sericite (illite) could likely be detrital in origin but its nonexistence in the uncemented intervals suggests in situ formation related to hydrothermal fluids.

The source of the heat is presumably the magmatic sill intrusions penetrating the sediments at several levels. The magmatic sill intrusions are generally not sufficiently thick to thermally affect the entire sequence because the thickness of the sedimentary strata that could be affected by thermal heat generated by the sill intrusions due to conduction according to most estimates is approximately twice the width of the sill (Dow, 1977; Peters et al., 1978; Karlsen et al., 1998; Brekke et al., 2014). However, intrusion into shallow highly porous sediments can create hydrothermal convection cells, which is the most effective way of dissipating the excess energy (Einsele et al., 1980).

Fluid flow due to sill emplacement will most likely initiate close to the top of the gently dipping sill surface and also likely under the sill. This will be at either tip of the sill since sills tend to be saucer shaped structures (Jamtveit et al., 2004) and under the sill due to build-up of high fluid pressures sufficient to trigger fluid mobilization. The prevalent geometry of the igneous intrusions emplaced during the early Cretaceous has been identified as saucer-shaped in central Spitsbergen (Senger et al., 2013). This would explain why the sandstone strata has been altered only in areas where

Table 1
$\delta^{13}C$ and $\delta^{18}O$ pore-filling calcite cement stable isotope analyses for samples of upper Triassic to Lower Jurassic sediments from Wilhelmøya, Svalbard.

Sample	$\delta^{13}C_{V\text{-}PDB}$, Calcite	$\delta^{18}O_{V\text{-}PDB}$, Calcite	Z-values
DF-3	-7.5	-13.3	105
DF-4	-10.2	-19.1	97
WS-3	-9.7	-20.6	97
WS-4	-8.8	-18.8	100

permeability differences resulting from existing carbonate cemented layers has led to channeling of the hydrothermal fluids.

The heat perturbation related to the emplacement of relatively small sill bodies is short-lived (Galland et al., 2006; Parnell, 2010). However, the reactivity of the pore water will be highly enhanced when mixed with heated hydrothermal fluids because this may lead to undersaturation with respect to carbonates. This will then induce dissolution followed by precipitation of the carbonates whose dissolution-precipitation kinetics is known to be fast. As mentioned above, the diagenetic fingerprints of most of the highly permeable sedimentary succession and the vitrinite reflectance indicate that the sandstones have not been subjected to higher temperature. Only the low permeable calcite cemented intervals that have been exposed to the hydrothermal pore water flow, contain high temperature diagenetic phases. Based on the above observation, we proposed that buoyant fluids have been partly following tight carbonate cemented flow baffles, before migrating into the sedimentary strata (Fig. 13A). On a local scale, the amount of calcite cement in each cemented intervals vary (Fig. 13B). The observations of hydrothermal induced diagenesis associated with the cemented sedimentary strata both close (~1 m) and far away (~65 m) from the sill suggest hydrothermal fluid mobility through the strata (Fig. 13).

The main effect of the hydrothermal fluids is recrystallization of already existing carbonates, and localized formation of hydrothermal albite, illite and sericite. Most likely, the carbonate containing layers lost their remaining porosity due to the hydrothermal activity but these layers must already have been flow baffles before the magmatic intrusions were emplaced. Identification of fluid pathways both vertical and lateral has not been done in the investigated area. Fluid movement resulting from sill emplacements should be studied further in the area in order to elucidate possible flow patterns generated by sills better.

5.4. Implications of sill intrusions on reservoir quality

The hydrothermal fluids injected into cooler host rocks due to sill intrusion emplacement may have impacts on porosity

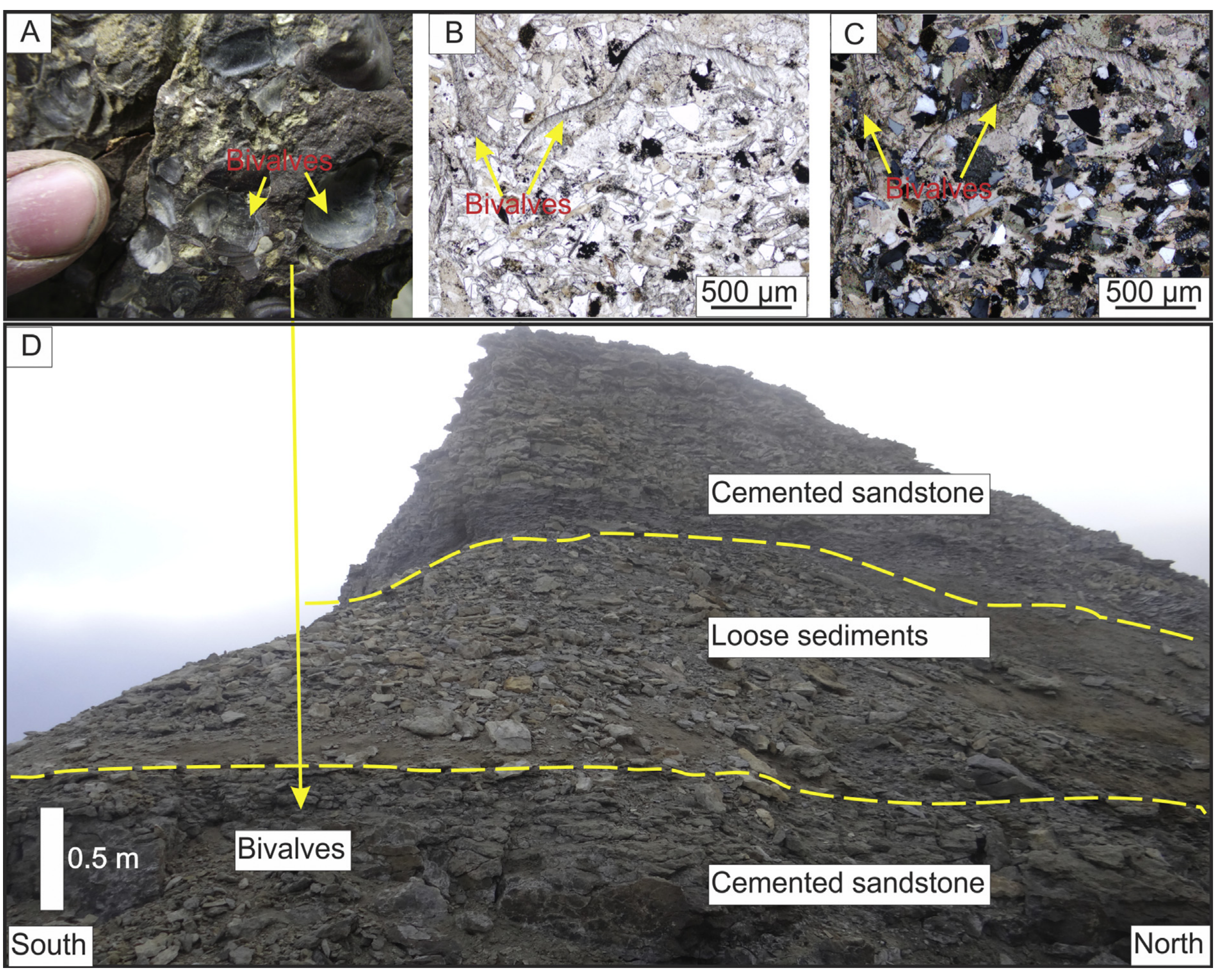

Figure 12. The sample and outcrop is from Wilhelmøya subgroup at Wilhelmøya. (A) Picture of hand sample showing bivalves. (B, C) Optical micrographs showing the distribution of bioclasts (bivalves) and carbonate cements at thin section scale. The calcite cement replaces bioclasts. (D) A picture of an outcrop section showing thin carbonate cemented layers with bivalves at the bottom, loosely cemented layers in the middle and thick carbonate cemented layers at the top. The location of outcrop section is eastern Wilhelmøya (79.06825°N and 20.72986°E) and view is westward. B is picture taken in plane polarized light while C in cross-polarized light.

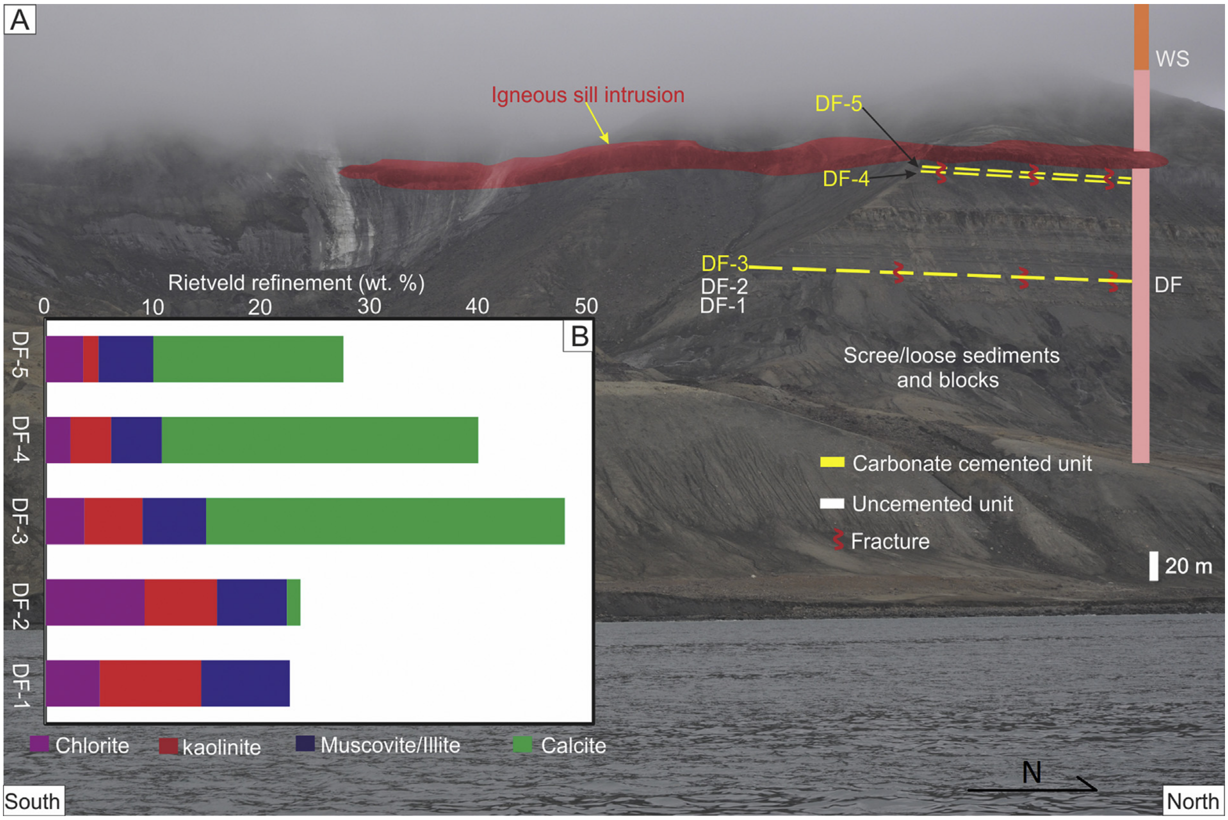

Figure 13. (A) Showing layer superimposed with red colored transparency is a mafic Early Cretaceous intrusion (ca. 124.5 Ma) that is cutting through Triassic strata (De Geerdalen Formation) along the eastern shores of Wilhelmøya (ca. 3.5 km east of Tumlingodden locality), Svalbard. The location of cliff section is eastern Wilhelmøya (79.08144°N and 20.68276°E) and view is westward. The intrusion is sub-parallel to layering for most of its length. Sampling locations of the hosting sedimentary layers are indicated with sample codes (DF-1 to DF-5). The samples were collected from both carbonate cemented and uncemented layers. (B) Histogram displays results of quantitative XRD Bulk mineralogy of DF-1 to DF-5 for primarily showing the variation of weight percent of calcite in the cemented intervals.

distribution (Einsele et al., 1980; Holford et al., 2013; Senger et al., 2014). The data presented above show that diagenetic reactions related to hydrothermal fluid flow related to sill emplacement were observed in carbonate-cemented intervals only. No apparent diagenetic effects like porosity decrease related to the sill emplacement was observed within intervals lacking carbonate cements. This is in accordance with earlier findings where the total porosity even as close as a few centimeters from the sill intrusion was unaffected by contact diagenesis (Mckinley et al., 2001; Grove, 2014; Grove et al., 2017). However, the hydrothermal fluid flow set up by the sill intrusion affected already existing flow barriers or baffles related to carbonate cemented layers. This lead to recrystallization and possibly increased cementation along already cemented intervals resulting in increased reservoir compartmentalization. Increased compartmentalization due to recrystallization should be considered since thin carbonate cemented layers and/or shale layers might exist in many siliciclastic reservoir rocks. This observation can be extended to any sedimentary basin where interbedded sandstone with thin carbonate or shale layers is common. Porosity will probably be reduced within the cemented layers after recrystallization while the reservoir quality outside the recrystallized zones will probably not be affected significantly.

6. Conclusion

Investigating impact of igneous intrusions on reservoir properties is important in order to evaluate their impact on the hydrocarbon potential of the northwestern Barents Sea and sedimentary basins elsewhere. In this study, the influence of sill intrusions on diagenesis and hence reservoir quality was evaluated.

Diagenetic evidences show that the upper Triassic and lower Jurassic sandstones at Wilhelmøya may be divided into intervals with different thermal histories; one being the bulk sediment, being largely unconsolidated and with a maximum burial temperature much lower than about 60–70 °C; and the second being thinner intervals that have experienced higher temperatures related to hydrothermal activity. The hydrothermally altered intervals are all tightly carbonate cemented layers. These intervals were most likely already carbonate cemented before the hydrothermal activity commenced, and would therefore have been flow baffles during the hydrothermal activity and thereby partly controlling the migration pathways of the buoyant hot fluids.

The hydrothermal fluid flow set up by the magmatic sill intrusions have affected the carbonate cemented sandstone intervals both close to the sill (~1 m) and away (~65 m) from the sill intrusion. The carbonate cemented intervals revealed high temperature hydrothermal induced reactions such as recrystallization of carbonate cements, localized sericitization of feldspars, albitization of both feldspar and plagioclase, and formation of fibrous illite nucleated on kaolinite. Within the intervals not affected by hydrothermal activity, there was no indication of hydrothermal induced diagenetic changes. This implies that the sill intrusion emplacement has not affected the porosity of these intervals.

Most of the available literature has focused on the effect of sill intrusion through conduction only. This work shows that igneous sill intrusion can also affect host rock intervals due to heat transfer through fluid flow. Possible hydrothermal fluid convection cells resulting from emplacement of sills should therefore be assessed together with conduction heat transfer when the influence of sill intrusions on reservoir quality is evaluated. The results from this study are applicable to the more general case of sedimentary basins having equivalent settings to the Wilhelmøya sediments.

Performing numerical modeling regarding the hydrothermal convection cell is beyond the scope of this study; however, the results obtained from this study could likely serve as inputs to perform such type of modeling in a future study. This will allow performing mass and energy balance calculations in order to understand the interplay between porous and permeable sediments and magmatic intrusions. This may enhance our quantitative predictive ability regarding reservoir quality evolution in such settings.

Acknowledgements

This work has been (partially) funded by the project "Reconstructing the Triassic Northern Barents shelf; basin infill patterns controlled by gentle sags and faults" (Trias North-www.mn.uio.no/triasnorth/) under grant 234152 from the Research Council of Norway and with financial support from Tullow Oil Norge, Lundin Norway, Statoil Petroleum, Edison Norge and RWE Dea Norge. We would like to thank reviewer Clayton Grove and anonymous reviewer, for constructive and insightful comments, which significantly improved an earlier version of the manuscript. Associate Editor Dr. Nick Roberts is also kindly thanked for editorial handling of the manuscript by giving his invaluable time. We are immensely thankful to Knut Bjørlykke for sharing his wealth of wisdom in diagenesis with us during the course of this research. We thank Maarten Aerts and Berit Løken Berg for guidance and assistance during the XRD and SEM work, respectively. We are also grateful to Kim Senger and Mark Mulrooney from Department of Arctic geology, University Centre in Svalbard, Norway and Kei Ogata from Vrije University, Amsterdam, Holland, for sharing their knowledge regarding the effect of sill intrusion emplacement on fluid flow in country rocks. Moreover, Mark Mulrooney and Kei Ogata are thanked for providing us quality outcrop pictures and for assistance during fieldwork. We would also like to thank Yingchang Cao from University of petroleum, Qingdao, China for allowing us to use their facility to perform fluid inclusion analyses on quartz and carbonate cement.

Appendix A. Supplementary data

Supplementary data related to this article can be found at https://doi.org/10.1016/j.gsf.2018.02.015.

References

Aagaard, P., Jahren, J., Harstad, A., Nilsen, O., Ramm, M., 2000. Formation of grain-coating chlorite in sandstones. Laboratory synthesized vs. natural occurrences. Clay Minerals 35, 261–269.

Aarnes, I., Svensen, H., Polteau, S., Planke, S., 2011. Contact metamorphic devolatilization of shales in the Karoo Basin, South Africa, and the effects of multiple sill intrusions. Chemical Geology 281, 181–194.

Aase, N.E., Bjorkum, P.A., Nadeau, P.H., 1996. The effect of grain-coating microquartz on preservation of reservoir porosity. AAPG Bulletin 80, 1654–1673.

Ahmed, W., 2002. Effects of heat-flow and hydrothermal fluids from volcanic intrusions on authigenic mineralization in sandstone formations. Bulletin of the Chemical Society of Ethiopia 16, 37–52.

Ajdukiewicz, J.M., Lander, R.H., 2010. Sandstone reservoir quality prediction: the state of the art. AAPG Bulletin 94, 1083–1091.

Anell, I., Braathen, A., Olaussen, S., Osmundsen, P., 2013. Evidence of faulting contradicts a quiescent northern Barents Shelf during the Triassic. First Break 31, 67–76.

Anell, I., Faleide, J., Braathen, A., 2016. Regional tectono-sedimentary development of the highs and basins of the northwestern barents shelf. Norwegian Journal of Geology 96, 27–41.

Angkasa, S.S., Jerram, D.A., Millett, J.M., Svensen, H.H., Planke, S., Taylor, R.A., Schofield, N., Howell, J., 2017. Mafic intrusions, hydrothermal venting, and the basalt-sediment transition: linking onshore and offshore examples from the North Atlantic igneous province. Interpretation 5 (3), Sk83–Sk101.

Antonsen, P., Elverhoi, A., Dypvik, H., Solheim, A., 1991. Shallow bedrock geology of the Olga basin area, northwestern Barents Sea (1). AAPG Bulletin 75, 1178–1194.

Barker, C.E., Pawlewicz, M.J., 1994. Calculation of vitrinite reflectance from thermal histories and peak temperatures-a comparison of methods. Vitrinite Reflectance as a Maturity Parameter 570, 216–229.

Bauer, A., Velde, B., Gaupp, R., 2000. Experimental constraints on illite crystal morphology. Clay Minerals 35, 587–597.

Bjølykke, K., 1980. Clastic diagenesis and basin evolution. Revista del Instituto de invetigaciones geologicas, Diputacion provincial, Universidad de Barcelona 21–44.

Bjørlykke, K., 1988. Sandstone diagenesis in relation to preservation, destruction and creation of porosity. Developments in Sedimentology 41, 555–588.

Bjørlykke, K., Elverhøi, B.A., Malm, A., 1979. Diagenesis in mesozoic sandstones from spitsbergen and the north Sea—a comparison. Geologische Rundschau 68, 1152–1171.

Bjørlykke, K., Jahren, J., 2012. Open or closed geochemical systems during diagenesis in sedimentary basins: constraints on mass transfer during diagenesis and the prediction of porosity in sandstone and carbonate reservoirs. AAPG Bulletin 96, 2193–2214.

Bjørlykke, K., Jahren, J., 2015. Sandstones and Sandstone Reservoirs, Petroleum Geoscience. Springer Berlin Heidelberg, pp. 113–140.

Blinova, M., Faleide, J.I., Gabrielsen, R.H., Mjelde, R., 2013. Analysis of structural trends of sub-sea-floor strata in the Isfjorden area of the West Spitsbergen Fold-and-Thrust belt based on multichannel seismic data. Journal of the Geological Society 170, 657–668.

Bloch, S., Lander, R.H., Bonnell, L., 2002. Anomalously high porosity and permeability in deeply buried sandstone reservoirs: origin and predictability. AAPG Bulletin 86, 301–328.

Blomeier, D., Wisshak, M., Dallmann, W., Volohonsky, E., Freiwald, A., 2003. Facies analysis of the old red Sandstone of spitsbergen (wood bay formation): reconstruction of the depositional environments and implications of basin development. Facies 49, 151–174.

Bodnar, R.J., 2003. Reequilibration of fluid inclusions. Fluid Inclusions: Analysis and Interpretation 32, 213–230.

Boles, J., Ramseyer, K., 1988. Albitization of Plagioclase and Vitrinite Reflectance as Paleothermal Indicators, San Joaquin Basin.

Braathen, A., Osmundsen, P.T., Maher, H., Ganerød, M., 2017. The Keisarhjelmen detachment records Silurian–Devonian extensional collapse in Northern Svalbard. Terra Nova 30, 34–39.

Breivik, A.J., Faleide, J.I., Gudlaugsson, S.T., 1998. Southwestern Barents Sea margin: late Mesozoic sedimentary basins and crustal extension. Tectonophysics 293, 21–44.

Brekke, T., Krajewski, K.P., Hubred, J.H., 2014. Organic geochemistry and petrography of thermally altered sections of the middle triassic botneheia formation on south-western Edgeøya, Svalbard. Norwegian Petroleum Directorate Bulletin 11, 111–128.

Bue, E.P., Andresen, A., 2013. Constraining depositional models in the Barents Sea Region using detrital Zircon U–Pb data from mesozoic sediments in Svalbard. Geological Society, London, Special Publications 386, 261–279.

Chuhan, F.A., Kjeldstad, A., Bjørlykke, K., Høeg, K., 2002. Porosity loss in sand by grain crushing—experimental evidence and relevance to reservoir quality. Marine and Petroleum Geology 19, 39–53.

Ditchfield, P.W., 1997. High northern palaeolatitude Jurassic-Cretaceous palaeotemperature variation: new data from Kong Karls Land, svalbard. Palaeogeography, Palaeoclimatology, Palaeoecology 130, 163–175.

Döbelin, N., 2015. PROFEX: Open Source XRD and Rietveld Refinement.

Dörr, N., Clift, P., Lisker, F., Spiegel, C., 2013. Why is Svalbard an island? Evidence for two-stage uplift, magmatic underplating, and mantle thermal anomalies. Tectonics 32, 473–486.

Dörr, N., Lisker, F., Clift, P., Carter, A., Gee, D.G., Tebenkov, A., Spiegel, C., 2012. Late Mesozoic–Cenozoic exhumation history of northern Svalbard and its regional significance: constraints from apatite fission track analysis. Tectonophysics 514, 81–92.

Dott Jr., R.H., 1964. Wacke, graywacke and matrix—what approach to immature Sandstone classification? Journal of Sedimentary Research 34.

Dow, W.G., 1977. Kerogen studies and geological interpretations. Journal of Geochemical Exploration 7, 79–99.

Dypvik, H., Håkansson, E., Heinberg, C., 2002. Jurassic and Cretaceous palaeogeography and stratigraphic comparisons in the North Greenland-Svalbard region. Polar Research 21, 91–108.

Ehrenberg, S., 1993. Preservation of anomalously high porosity in deeply buried sandstones by grain-coating chlorite: examples from the Norwegian continental shelf. AAPG Bulletin 77, 1260–1286.

Eide, C.H., Schofield, N., Jerram, D.A., Howell, J.A., 2017. Basin-scale architecture of deeply emplaced sill complexes: Jameson Land, East Greenland. Journal of the Geological Society 174, 23–40.

Einsele, G., 2013. Sedimentary Basins: Evolution, Facies, and Sediment Budget. Springer Berlin Heidelberg.

Einsele, G., Gieskes, J.M., Curray, J., Moore, D.M., Aguayo, E., Aubry, M.-P., Fornari, D., Guerrero, J., Kastner, M., Kelts, K., Lyle, M., Matoba, Y., Molina-Cruz, A., Niemitz, J., Rueda, J., Saunders, A., Schrader, H., Simoneit, B., Vacquier, V., 1980. Intrusion of basaltic sills into highly porous sediments, and resulting hydrothermal activity. Nature 283, 441–445.
Faleide, J.I., Bjørlykke, K., Gabrielsen, R.H., 2015. Geology of the Norwegian Continental Shelf, Petroleum Geoscience. Springer, pp. 603–637.
Faleide, J.I., Gudlaugsson, S.T., Jacquart, G., 1984. Evolution of the western Barents Sea. Marine and Petroleum Geology 1, 123–150.
Faleide, J.I., Tsikalas, F., Breivik, A.J., Mjelde, R., Ritzmann, O., Engen, O., Wilson, J., Eldholm, O., 2008. Structure and evolution of the continental margin off Norway and the Barents Sea. Episodes 31, 82.
Faleide, J.I., Vågnes, E., Gudlaugsson, S.T., 1993. Late Mesozoic-Cenozoic evolution of the south-western Barents Sea in a regional rift-shear tectonic setting. Marine and Petroleum Geology 10, 186–214.
Ferry, J.M., Dipple, G.M., 1991. Fluid flow, mineral reactions, and metasomatism. Geology 19, 211–214.
Folk, R.L., Andrews, P.B., Lewis, D., 1970. Detrital sedimentary rock classification and nomenclature for use in New Zealand. New Zealand Journal of Geology and Geophysics 13, 937–968.
Friedman, I., O'Neil, J.R., 1977. Compilation of Stable Isotope Fractionation Factors of Geochemical Interest. USGPO.
Gabrielsen, R., 1984. Long-lived fault zones and their influence on the tectonic development of the southwestern Barents Sea. Journal of the Geological Society 141, 651–662.
Galland, O., Cobbold, P.R., Hallot, E., de Bremond d'Ars, J., Delavaud, G., 2006. Use of vegetable oil and silica powder for scale modelling of magmatic intrusion in a deforming brittle crust. Earth and Planetary Science Letters 243, 786–804.
Genthon, P., Rabinowicz, M., Foucher, J.P., Sibuet, J.C., 1990. Hydrothermal circulation in an anisotropic sedimentary basin: application to the Okinawa back arc basin. Journal of Geophysical Research: Solid Earth 95, 19175–19184.
Gjelberg, J., Steel, R., 1981. An outline of Lower-Middle Carboniferous sedimentation on Svalbard: effects of tectonic, climatic and sea level changes in rift basin sequences. In: Fergusson, A.J., Kerr, J.W. (Eds.), Geology of the North Atlantic Borderlands. Canadian Society of Petroleum Geologists. Alberta, Calgary, pp. 543–561.
Glørstad-Clark, E., Birkeland, E., Nystuen, J., Faleide, J., Midtkandal, I., 2011. Triassic platform-margin deltas in the western Barents Sea. Marine and Petroleum Geology 28, 1294–1314.
Glørstad-Clark, E., Faleide, J.I., Lundschien, B.A., Nystuen, J.P., 2010. Triassic seismic sequence stratigraphy and paleogeography of the western Barents Sea area. Marine and Petroleum Geology 27, 1448–1475.
González-Acebrón, L., Goldstein, R.H., Mas, R., Arribas, J., 2011. Criteria for recognition of localization and timing of multiple events of hydrothermal alteration in sandstones illustrated by petrographic, fluid inclusion, and isotopic analysis of the Tera Group, Northern Spain. International Journal of Earth Sciences 100, 1811–1826.
Grapes, R., 2010. Pyrometamorphism. Springer Science & Business Media.
Grigsby, J.D., 2001. Origin and growth mechanism of authigenic chlorite in sandstones of the lower Vicksburg Formation, south Texas. Journal of Sedimentary Research 71, 27–36.
Grove, C., 2013. Submarine hydrothermal vent complexes in the Paleocene of the Faroe-Shetland Basin: insights from three-dimensional seismic and petrographical data. Geology 41, 71–74.
Grove, C., 2014. Direct and Indirect Effects of Flood Basalt Volcanism on Reservoir Quality Sandstone. Durham University.
Grove, C., Jerram, D., Gluyas, J., Brown, R., 2017. Sandstone diagenesis in Sediment–lava Sequences: Exceptional examples of volcanically driven diagenetic compartmentalization in Dune Valley, Huab Outliers, Nw Namibia. Journal of Sedimentary Research 87, 1314–1335.
Gustavsen, F.B., Dypvik, H., Solheim, A., 1997. Shallow geology of the northern Barents Sea: implications for petroleum potential. AAPG Bulletin 81, 1827–1842.
Haile, B.G., Hellevang, H., Aagaard, P., Jahren, J., 2015. Experimental nucleation and growth of smectite and chlorite coatings on clean feldspar and quartz grain surfaces. Marine and Petroleum Geology 68, 664–674.
Haile, B.G., Klausen, T.G., Jahren, J., Braathen, A., Hellevang, H., in press. Thermal history of a Triassic sedimentary sequence verified by a multi-method approach: Edgeøya, Svalbard, Norway. Basin Research.
Hallam, A., 1985. A review of Mesozoic climates. Journal of the Geological Society 142, 433–445.
Hellevang, H., Haile, B.G., Tetteh, A., 2017. Experimental study to better understand factors affecting the CO_2 mineral trapping potential of basalt. Greenhouse Gases: Science and Technology 7, 143–157.
Henriksen, E., Bjørnseth, H., Hals, T., Heide, T., Kiryukhina, T., Kløvjan, O., Larssen, G., Ryseth, A., Rønning, K., Sollid, K., 2011. Uplift and erosion of the greater Barents Sea: impact on prospectivity and petroleum systems. Geological Society, London, Memoirs 35, 271–281.
Holford, S., Schofield, N., Jackson, C.-L., Magee, C., Green, P., Duddy, I., 2013. Impacts of Igneous Intrusions on Source Reservoir Potential in Prospective Sedimentary Basins along the Western Australian Continental Margin.
Holford, S., Schofield, N., MacDonald, J., Duddy, I., Green, P., 2012. Seismic analysis of igneous systems in sedimentary basins and their impacts on hydrocarbon prospectivity: examples from the southern Australian margin. The APPEA Journal 52, 229–252.
Hower, J., Eslinger, E.V., Hower, M.E., Perry, E.A., 1976. Mechanism of burial metamorphism of argillaceous sediment: 1. Mineralogical and chemical evidence. Geological Society of America Bulletin 87, 725–737.
Jamtveit, B., Svensen, H., Podladchikov, Y.Y., Planke, S., 2004. Hydrothermal vent complexes associated with sill intrusions in sedimentary basins. Physical Geology of High-Level Magmatic Systems 234, 233–241.
Jerram, D., 2015. Hot rocks and oil: are volcanic margins the new frontier. Exploration & Production. Geofacets, Elsevier, Amsterdam. https://www.elsevier.com/__data/assets/pdf_file/0008/84887/ELS_Geofacets-Volcanic-Article_Digital_r5.pdf.
Johansen, S., Ostisty, B., Birkeland, Ø., Fedorovsky, Y., Martirosjan, V., Christensen, O.B., Cheredeev, S., Ignatenko, E., Margulis, L., 1992. Hydrocarbon potential in the Barents Sea region: play distribution and potential. Arctic Geology and Petroleum Potential, Norwegian Petroleum Society (NPF), Special Publication 2, 273–320.
Johansson, Å., Gee, D.G., Larionov, A.N., Ohta, Y., Tebenkov, A.M., 2005. Grenvillian and Caledonian evolution of eastern Svalbard–a tale of two orogenies. Terra Nova 17, 317–325.
Karlsen, D., Dahlgren, S., Jarntveit, B., Kjærnet, T., 1998. Thermal effects of basaltic sill emplacement in Source rocks for maturation and hydrocarbon generation. In: 60th EAGE Conference & Exhibition.
Keith, M., Weber, J., 1964. Carbon and oxygen isotopic composition of selected limestones and fossils. Geochimica et Cosmochimica Acta 28, 1787–1816.
Klausen, T., Mørk, A., 2014. The upper triassic paralic deposits of the de Geerdalen Formation on Hopen: outcrop analog to the subsurface snadd formation in the Barents Sea. AAPG Bulletin 98, 1911–1941.
Klausen, T.G., Ryseth, A.E., Helland-Hansen, W., Gawthorpe, R., Laursen, I., 2014. Spatial and temporal changes in geometries of fluvial channel bodies from the triassic snadd formation of offshore Norway. Journal of Sedimentary Research 84, 567–585.
Klausen, T.G., Ryseth, A.E., Helland-Hansen, W., Gawthorpe, R., Laursen, I., 2015. Regional development and sequence stratigraphy of the middle to late triassic snadd formation, Norwegian Barents Sea. Marine and Petroleum Geology 62, 102–122.
Krajewski, K.P., 2008. The botneheia formation (middle triassic) in Edgeøya and barentsøya, svalbard: lithostratigraphy, facies, phosphogenesis, paleoenvironment. Polish Polar Research 29, 319–364.
Lander, R.H., Bonnell, L.M., 2010. A model for fibrous illite nucleation and growth in sandstones. AAPG Bulletin 94, 1161–1187.
Lord, G.S., Johansen, S.K., Støen, S.J., Mørk, A., 2017. Facies development of the upper triassic succession on barentsøya, Wilhelmøya and NE spitsbergen, svalbard. Norwegian Journal of Geology/Norsk Geologisk Forening 97.
Lord, G.S., Solvi, K.H., Klausen, T.G., Mørk, A., 2014. Triassic channel bodies on Hopen, Svalbard: their facies, stratigraphic significance and spatial distribution. Norwegian Petroleum Directorate 11, 41–59. Stavanger.
Lundschien, B.A., Høy, T., Mørk, A., 2014. Triassic hydrocarbon potential in the Northern Barents Sea; integrating Svalbard and stratigraphic core data. Norwegian Petroleum Directorate Bulletin 11, 3–20.
Machel, H.G., Lonnee, J., 2002. Hydrothermal dolomite—a product of poor definition and imagination. Sedimentary Geology 152, 163–171.
Maher Jr., H.D., 2001. Manifestations of the Cretaceous high arctic large igneous province in svalbard. The Journal of Geology 109, 91–104.
McBride, E.F., 1963. A classification of common sandstones. Journal of Sedimentary Research 33.
Mckinley, J.M., Worden, R.H., Ruffell, A.H., 2001. Contact diagenesis: the effect of an intrusion on reservoir quality in the triassic sherwood Sandstone group, northern Ireland. Journal of Sedimentary Research 71, 484–495.
Meunier, A., Velde, B., 1982. Phengitization, sericitization and potassium-beidellite in a hydrothermally altered granite. Clay Minerals 17, 285–299.
Morad, S., Al-Ramadan, K., Ketzer, J.M., De Ros, L., 2010. The impact of diagenesis on the heterogeneity of sandstone reservoirs: a review of the role of depositional facies and sequence stratigraphy. AAPG Bulletin 94, 1267–1309.
Morad, S., Bergan, M., Knarud, R., Nystuen, J.P., 1990. Albitization of detrital plagioclase in triassic reservoir sandstones from the snorre field, Norwegian North Sea. Journal of Sedimentary Research 60.
Moraes, M.A., De Ros, L.F., 1990. Infiltrated clays in fluvial Jurassic sandstones of Recôncavo Basin, northeastern Brazil. Journal of Sedimentary Research 60.
Mørk, A., Bjorøy, M., 1984. Mesozoic Source Rocks on Svalbard, Petroleum Geology of the North European Margin. Springer, pp. 371–382.
Mørk, A., Embry, A.F., Weitschat, W., 1989. Triassic Transgressive-regressive Cycles in the Sverdrup Basin, Svalbard and the Barents Shelf, Correlation in Hydrocarbon Exploration. Springer, pp. 113–130.
Mørk, A., Dallmann, W., Dypvik, H., Johannessen, E., Larssen, G., Nagy, J., Nøttvedt, A., Olaussen, S., Pchelina, T., Worsley, D., 1999. Mesozoic lithostratigraphy. In: Dallmann, W.k. (Ed.), Lithostratigraphic lexicon of Svalbard. Review and recommendations for nomenclature use. Upper Palaeozoic to Quaternary bedrock. Norwegian Polar Institute, Tromsø, pp. 127–214.
Mørk, M.B.E., 1999. Compositional variations and provenance of triassic sandstones from the Barents Shelf. Journal of Sedimentary Research 69, 690–710.
Mørk, M.B.E., 2013. Diagenesis and quartz cement distribution of low-permeability Upper Triassic–Middle Jurassic reservoir sandstones, Longyearbyen CO_2 lab well site in Svalbard, Norway. AAPG Bulletin 97, 577–596.
Nejbert, K., Krajewski, K.P., Dubińska, E., Pécskay, Z., 2011. Dolerites of svalbard, north-west Barents Sea Shelf: age, tectonic setting and significance for geotectonic interpretation of the high-arctic large igneous province. Polar Research 30.

Nøttvedt, A., Berglund, L., Rasmussen, E., Steel, R., 1988. Some aspects of tertiary tectonics and sedimentation along the Western Barents Shelf. Geological Society, London, Special Publications 39, 421–425.

Nøttvedt, A., Cecchi, M., Gjelberg, J., Kristensen, S., Lønøy, A., Rasmussen, A., Rasmussen, E., Skott, P., Van Veen, P., 1992. Svalbard-Barents Sea correlation: a short review. Arctic Geology and Petroleum Potential, Norwegian Petroleum Society (NPF), Special Publication 2, 363–375.

Nyland, B., Jensen, L., Skagen, J., Skarpnes, O., Vorren, T., 1992. Tertiary uplift and erosion in the Barents Sea: magnitude, timing and consequences. In: Larsen, R.M., Brekke, H., Larsen, B.T., Talleraas, E. (Eds.), Structural and Tectonic Modelling and its Application to Petroleum Geology, Norwegian Petrol. Soc. Spec. Publ, pp. 153–162.

Ochoa, M., Arribas, J., Mas, R., Goldstein, R., 2007. Destruction of a fluvial reservoir by hydrothermal activity (Cameros Basin, Spain). Sedimentary Geology 202, 158–173.

Parnell, J., 2010. Potential of palaeofluid analysis for understanding oil charge history. Geofluids 10, 73–82.

Peters, K., Simoneit, B., Brenner, S., Kaplan, I., 1978. Vitrinite Reflectance-temperature Determinations for Intruded Cretaceous Black Shale in the Eastern Atlantic, Symposium in Geochemistry: Low Temperature Metamorphism of Kerogen and Clay Minerals. Society for Sedimentary Geology.

Pettijohn, F.J., Potter, P.E., Siever, R., 2012. Sand and Sandstone. Springer Science & Business Media.

Pittman, E.D., Larese, R.E., Heald, M.T., 1992. Clay coats: Occurrence and Relevance to Preservation of Porosity in Sandstones.

Polteau, S., Hendriks, B.W., Planke, S., Ganerød, M., Corfu, F., Faleide, J.I., Midtkandal, I., Svensen, H.S., Myklebust, R., 2016. The early Cretaceous Barents Sea Sill complex: distribution, $^{40}Ar/^{39}Ar$ geochronology, and implications for carbon gas formation. Palaeogeography, Palaeoclimatology, Palaeoecology 441, 83–95.

Que, M., Allen, A.R., 1996. Sericitization of plagioclase in the Rosses granite complex, Co. Donegal, Ireland. Mineralogical Magazine 60, 927–936.

Rateau, R., Schofield, N., Smith, M., 2013. The potential role of igneous intrusions on hydrocarbon migration, West of Shetland. Petroleum Geoscience 19, 259–272.

Reeckmann, S., Duddy, I., Gleadow, A., 1985. Igneous intrusions in porous Sandstone Sequences–widespread thermal effects measured by fission track annealing and Vitrinite reflectance: ABSTRACT. AAPG Bulletin 69, 299–300.

Riis, F., Lundschien, B.A., Høy, T., Mørk, A., Mørk, M.B.E., 2008. Evolution of the triassic shelf in the northern Barents Sea region. Polar Research 27, 318–338.

Rød, R.S., Hynne, I.B., Mørk, A., 2014. Depositional environment of the upper triassic de Geerdalen Formation–An EW transect from Edgeøya to central spitsbergen, svalbard. Norwegian Petroleum Directorate Bulletin 11, 21–40.

Rossi, C., Goldstein, R.H., Ceriani, A., Marfil, R., 2002. Fluid inclusions record thermal and fluid evolution in reservoir sandstones, Khatatba Formation, Western Desert, Egypt: a case for fluid injection. AAPG Bulletin 86.

Salem, A.M., Morad, S., Mato, L.F., Al-Aasm, I., 2000. Diagenesis and reservoir-quality evolution of fluvial sandstones during progressive burial and uplift: evidence from the upper Jurassic boipeba member, reconcavo basin, northeastern Brazil. AAPG Bulletin 84, 1015–1040.

Sanderson, I.D., 1984. Recognition and significance of inherited quartz overgrowths in quartz arenites. Journal of Sedimentary Research 54.

Schofield, N., Holford, S., Millett, J., Brown, D., Jolley, D., Passey, S.R., Muirhead, D., Grove, C., Magee, C., Murray, J., Hole, M., Jackson, C.A.L., Stevenson, C., 2015a. Regional magma plumbing and emplacement mechanisms of the Faroe-Shetland Sill Complex: implications for magma transport and petroleum systems within sedimentary basins. Basin Research 29, 41–63.

Schofield, N., Jerram, D.A., Holford, S., Archer, S., Mark, N., Hartley, A., Howell, J., Muirhead, D., Green, P., Hutton, D., Stevenson, C., 2015b. Sills in Sedimentary Basins and Petroleum Systems. Springer Berlin Heidelberg, Berlin, Heidelberg, pp. 1–22.

Schofield, N., Jolley, D., Holford, S., Archer, S., Watson, D., Hartley, A., Howell, J., Muirhead, D., Underhill, J., Green, P., 2017. Challenges of future exploration within the UK rockall basin. In: Geological Society, London, Petroleum Geology Conference Series, vol. 8.

Senger, K., Millett, J., Planke, S., Ogata, K., Eide, C.H., Festøy, M., Galland, O., Jerram, D.A., 2017. Effects of igneous intrusions on the petroleum system: a review. First Break 35, 47–56.

Senger, K., Roy, S., Braathen, A., Buckley, S.J., Bælum, K., Gernigon, L., Mjelde, R., Noormets, R., Ogata, K., Olaussen, S., 2013. Geometries of doleritic intrusions in central Spitsbergen, Svalbard: an integrated study of an onshore-offshore magmatic province with implications for CO_2 sequestration. Norwegian Journal of Geology 93, 3–4.

Senger, K., Tveranger, J., Ogata, K., Braathen, A., Planke, S., 2014. Late mesozoic magmatism in svalbard: a review. Earth-Science Reviews 139, 123–144.

Smith, A.G., Smith, D.G., Funnell, B.M., 1994. Atlas of Mesozoic and Cenozoic Coastlines. Cambridge University Press, Cambridge.

Sobolev, P., 2012. Cenozoic uplift and erosion of the Eastern Barents Sea–constraints from offshore well data and the implication for petroleum system modelling [Känozoische Hebung und Erosion der östlichen Barentssee–Abschätzungen aus Offshore-Bohrungsdaten und Auswirkung auf die Erdölsystem-Modellierung)]. Zeitschrift der Deutschen Gesellschaft für Geowissenschaften 163, 309–324.

Steel, R.J., Worsley, D., 1984. Patterns and palaeogeographic, petroleum geology of the north European margin. In: Proceedings of the North European Margin Symposium (NEMS'83), Organized by the Norwegian Petroleum Society and Held at the Norwegian Institute of Technology (NTH) in Trondheim 9–11 May, 1983. Springer Science & Business Media, p. 109.

Stemmerik, L., Worsley, D., 1989. Late Palaeozoic Sequence Correlations, North Greenland, Svalbard and the Barents Shelf, Correlation in Hydrocarbon Exploration. Springer, pp. 99–111.

Surdam, R.C., Boese, S.W., Crossey, L.J., 1983. The chemistry of secondary porosity: Part 2. Aspects of porosity modification. In: McDonald, D.A., C.Surdam, R. (Eds.), Clastic Diagenesis. American Association of Petroleum Geologists, pp. 127–149.

Sweeney, J.J., Burnham, A.K., 1990. Evaluation of a simple model of Vitrinite reflectance based on chemical kinetics (1). AAPG Bulletin 74, 1559–1570.

Taylor, T.R., Giles, M.R., Hathon, L.A., Diggs, T.N., Braunsdorf, N.R., Birbiglia, G.V., Kittridge, M.G., Macaulay, C.I., Espejo, I.S., 2010. Sandstone diagenesis and reservoir quality prediction: models, myths, and reality. AAPG Bulletin 94, 1093–1132.

Verati, C., Jourdan, F., 2014. Modelling effect of sericitization of plagioclase on the 40K/40Ar and 40Ar/39Ar chronometers: implication for dating basaltic rocks and mineral deposits. Geological Society, London, Special Publications 378, 155–174.

Vorren, T.O., Richardsen, G., Knutsen, S.-M., Henriksen, E., 1991. Cenozoic erosion and sedimentation in the western Barents Sea. Marine and Petroleum Geology 8, 317–340.

Walderhaug, O., 1994. Temperatures of quartz cementation in Jurassic sandstones from the Norwegian continental shelf–evidence from fluid inclusions. Journal of Sedimentary Research 64.

Weigand, P.W., Testa, S.M., 1982. Petrology and geochemistry of Mesozoic dolerites from the Hinlopenstretet area. Svalbard. Polar Research 1982, 35–52.

Weiss, H., Wilhelms, A., Mills, N., Scotchmer, J., Hall, P., Lind, K., Brekke, T., 2000. NIGOGA-The Norwegian Industry Guide to Organic Geochemical Analyses [Online]. Edition 4.0 Published by Norsk Hydro, Statoil, Geolab Nor, SINTEF Petroleum Research and the Norwegian Petroleum Directorate. pp. 102. Availabel at. http://www.npd.no/english/nigoga/nigoga.pdf.

Wilkinson, M., Haszeldine, R.S., 2002. Fibrous illite in oilfield sandstones – a nucleation kinetic theory of growth. Terra Nova 14, 56–60.

Williams, H., Turner, F.J., Gilbert, C.M., 1982. Petrography: an Introduction to the Study of Rocks in Thin Section. WH Freeman and Company.

Williams, L.A., Parks, G.A., Crerar, D.A., 1985. Silica diagenesis, I. Solubility controls. Journal of Sedimentary Research 55.

Wilson, J., Cressey, G., Cressey, B., Cuadros, J., Ragnarsdottir, K.V., Savage, D., Shibata, M., 2006. The effect of iron on montmorillonite stability. (II) Experimental investigation. Geochimica et Cosmochimica Acta 70, 323–336.

Wilson, J.C., McBride, E.F., 1988. Compaction and porosity evolution of pliocene sandstones, ventura basin, California. AAPG Bulletin 72, 664–681.

Wilson, M.D., Pittman, E.D., 1977. Authigenic clays in sandstones: recognition and influence on reservoir properties and paleoenvironmental analysis. Journal of Sedimentary Research 47.

Wilson, M.E., Evans, M.J., Oxtoby, N.H., Nas, D.S., Donnelly, T., Thirlwall, M., 2007. Reservoir quality, textural evolution, and origin of fault-associated dolomites. AAPG Bulletin 91, 1247–1272.

Worden, R., Morad, S., 2000. Quartz cementation in oil field sandstones: a review of the key controversies. Quartz cementation in sandstones. Special Publications of International Association of Sedimentologists 29, 1–20.

Worden, R., Morad, S., 2003. Clay minerals in Sandstones: Controls on Formation, Distribution and Evolution. Wiley Online Library.

Worsley, D., 1973. The Wilhelmøya Formation—a new lithostratigraphical unit from the Mesozoic of eastern Svalbard. Norsk Polarinstitutt Årbok 1971, 17–34.

Worsley, D., 2008. The post-Caledonian development of Svalbard and the western Barents Sea. Polar Research 27, 298–317.

Zhu, C., Veblen, D.R., Blum, A.E., Chipera, S.J., 2006. Naturally weathered feldspar surfaces in the Navajo Sandstone aquifer, Black Mesa, Arizona: electron microscopic characterization. Geochimica et Cosmochimica Acta 70, 4600–4616.